Order Number 9300343

The source of five-minute period photospheric umbral oscillations

Penn, Matthew James, Ph.D.

University of Hawaii, 1992

U·M·I
300 N. Zeeb Rd.
Ann Arbor, MI 48106

THE SOURCE OF FIVE-MINUTE PERIOD

PHOTOSPHERIC UMBRAL OSCILLATIONS

A DISSERTATION SUBMITTED TO THE GRADUATE DIVISION OF THE
UNIVERSITY OF HAWAII IN PARTIAL FULFILLMENT
OF THE REQUIREMENTS FOR THE DEGREE OF

DOCTOR OF PHILOSOPHY

IN ASTRONOMY

AUGUST 1992

By

Matthew James Penn

Dissertation Committee:

Barry LaBonte, Committee Chair
Richard Canfield
Charles Lindsey
James Heasley
Frederick A. Harris

This work is dedicated to my sister Dawn, and to my parents,

Susan and Wayne Penn.

ACKNOWLEDGEMENTS

I would like to thank my advisor, Barry LaBonte, for his guidance and advice, as well as the environment of independence he provided for me during this work. I thank Richard Canfield for being the driving force behind the construction of the MCCD instrument; without his perseverance during the project it is unlikely the instrument would be operating today. I owe a great deal to Donald Mickey, who designed the MCCD optical system, and who was a constant source of information and ideas during this work. Charles Lindsey, George Fisher, Doug Braun and many of the other members of the solar division of the University of Hawaii's Institute for Astronomy provided insightful comments during my dissertation, and I would like to offer a generous "Mahalo" to all the members of this group.

During the MCCD project, I would like to acknowledge the enormous contributions of Elaine Kiernan to the software of the MCCD, of Herb Ryerson to the design and fabrication of the fast guider electronics, and of Buzz Graves, for his design work, fabrication, installation, and general knowledge of the fast guider system. Dr. Jean-Pierre Wuelser made important contributions during the characterizations of the coronagraph and spectrograph, and resolved many of the initial problems with the MCCD system. Among the list of many who have contributed to the MCCD project in important ways include Darryl Koon, Tim Georges, Les Heida and Mark Waterson at the Mees Solar Observatory, and Dr. Tom Metcalf, and Chas Cavedoni at the Institute for Astronomy.

Among the graduate students at the IfA I would especially like to thank James Annis, Mike Rigler and Robert Ronan for constructive conversation, insightful comments, and a seemingly infinite supply of late night coffee. The companionship of the graduate students at the IfA helped to relieve the heavy burdens imposed by graduate school. I wish to thank all the graduate students at the IfA and wish them successful and satisfying futures.

I cannot begin to describe the generous support and understanding which Stevie Calandra gave to me during all the stages of this project. Her encouragement and perspective provided a stable base from which I could stand and face the demands of graduate school; without her companionship I would be incomplete. Among the many in Honolulu who helped to keep me sane are the members of the University of Hawaii Ultimate Frisbee Club, the runners in the Beer & Nacho's Track Club, and everyone at Andy's Manoa Health Food Market; mahalo and aloha!

I would like to express my sincere thanks to my family for the understanding and encouragement which they have shown during my years in school. I thank my sister Dawn for her understanding and patience, and wish her luck with her own new family. Above all others, I would like to thank my parents, Susan and Wayne Penn, for the constant encouragement and support which they have given me through all the stages of my life. Without the support and independence they gave to me none of this would have been possible.

Finally I offer thanks to Maui the demi-god. According to the rich folklore of ancient Hawaii, Maui battled the Sun-god, La, in the crater of the volcano Haleakala. The Sun had traveled too rapidly across the sky, making the day too short for the people of Hawaii to complete their daily tasks. Maui fiercely battled La, spilling his blood in the crater and giving Haleakala its red color. La reluctantly agreed to travel across the sky slowly during half of the year, allowing Hawaiians to make their living, and allowing solar astronomers to obtain long time series of data. Maui no ka oi!

ABSTRACT

Many types of velocity oscillations are observed in the umbrae and penumbrae of sunspots. We describe a project aimed at determining the source of one type of oscillation, the five-minute period photospheric umbra oscillations. The project uses imaging spectroscopy of spot umbrae, measuring the Doppler shift of pure umbral absorption lines to study the temporal and spatial properties of these oscillations.

The Mees CCD (MCCD) instrument is an imaging spectroscopy device which uses the 25 cm coronagraph telescope and the 3.0 m coude spectrograph at Mees Solar Observatory (MSO) on Haleakala, Maui. The instrument works with resolving power up to $R \approx 200{,}000$ with significant throughput from $\lambda 3934$ Å (Ca II K) to $\lambda \approx 10000$ Å. A fast guiding active mirror stabilizes the image during observations. A rapidly writing magnetic tape storage system allows observations to be recorded at 256 kbytes s^{-1}.

We observed the oscillations in the umbrae of two sunspots using the MCCD imaging spectrograph. We observed the Doppler shifts of 18 molecular lines in the umbrae for roughly 50 hours in each spot during the interval of 11 to 16 May 1991. We find no simple correlation between the velocity measured with molecular lines and the velocity measured using two iron lines. We remove solar rotation, image drift, and interpolate all the data onto an even time grid. We perform four spatial analyses of the umbral velocity and find (1) there is more power traveling toward the center of the umbrae than leaving the center of the umbrae (this provides a direct measure of the absorption of p-modes by the sunspot umbrae) (2) the umbral

oscillations have spatial and temporal characteristics indistinguishable from the quiet-sun oscillations, (3) a Fourier-Bessel analysis shows no obvious resonant frequencies which might represent natural oscillation modes of the sunspot umbrae, and (4) the centers of the umbrae have less RMS velocity than the edge of the umbrae. From these analyses we conclude that the photospheric umbral oscillations are driven by an external source and that source is the global p-mode oscillations.

TABLE OF CONTENTS

LIST OF TABLES

LIST OF ILLUSTRATIONS

CHAPTER 1

Introduction

Sunspots are dark regions on the solar surface which contain strong magnetic fields. Sunspots have complicated systems of quasi-stationary flows; horizontal and vertical flows are observed in the central umbra and penumbra. These flows are seen in the photosphere, the chromosphere, and even in the upper chromosphere and transition region. Flows are even observed in the quiet-sun surrounding sunspots. The structure and flow fields of sunspots are of great interest to solar physicists, and the reader is referred to several excellent reviews of sunspot structure and the velocity fields found in sunspots (for example see Moore 1981, Thomas 1981, Garcia de la Rosa 1981, Moore and Rabin 1985, and Lites 1992) for further details.

Sunspots also contain a variety of dynamic oscillatory phenomena. Oscillations in intensity and in the plasma velocity are observed in sunspots. In this chapter I will review what is known about the velocity oscillations in sunspots, examining the umbral and penumbral regions of the photosphere and chromosphere; and then briefly discuss some theories regarding the source and nature of these oscillations. (The reader is referred to the reviews mentioned above for details concerning the intensity oscillations seen in sunspots.) Next I discuss the general problems of observing velocity oscillations in sunspots and the advantages of using pure umbral absorption lines. Finally details about how oscillation observations can be used to examine the velocity

fields and the structure of sunspots are discussed.

1. Oscillations in and Around Sunspots

1.1. Umbral Oscillations

Beckers and Schultz (1972) observed umbral oscillations using a photospheric absorption line; they observed oscillations in the five-minute period band (roughly from 2.5 to 4.5 mHz) but suggested that these five-minute oscillations were simply contamination from the quiet-sun oscillations. However, Bhatnagar et al. (1972) unambiguously determined that the umbral oscillations are dominated by oscillation power in the five-minute frequency band. They used a pure umbral absorption line to remove the possibility of contamination from the much stronger oscillations in the photosphere. Subsequent observations of the umbral oscillations at the photospheric level have shown that the five-minute oscillations dominate the power spectrum. (Livingston and Mahaffey 1981, Thomas, Cram and Nye 1982, Soltau and Wiehr 1984, Abdelatif, Lites, Thomas 1986, Balthasar, Fangmeier, Kuveler and Wiehr 1988, Wiehr, Balthasar and Stellmacher 1988, Alamanni, Cavallini, Ceppatelli, and Righini 1990.)

The amplitude of the five-minute oscillations appear reduced inside the sunspot compared to the quiet sun. This has been known since the observations of Leighton, Noyes and Simon (1962); Lites (1992) states that the mean velocity inside the sunspot umbra (from numerous observations) is 75 m s^{-1} which implies that the oscillation amplitude is reduced by a factor of about 10 compared to the global p-mode oscilla-

tions. Theories explaining this power reduction (see Bogdan 1992) include only selective transmission of the global p-modes by sunspots, and coupling of the p-modes to unobservable oscillations by the sunspot magnetic field.

There is much debate concerning the spatial characteristics of the umbral oscillations. Lites (1992) states that the oscillations are coherent over a large area of the sunspot umbrae. This is apparently verified by Kobanov (1990) who claims that there is no spatial variation of the oscillations inside the sunspot, that the umbra oscillates as a single unit. Some results contradict this conclusion; for example Abdelatif et al. (1986) claim that the umbral oscillations represent a selective transmission of the quiet-sun p-modes having an acoustic phase velocity of 25 km s^{-1} or less. At the temporal frequency of $\nu = 3.2$ mHz, this would give a horizontal wavelength of about 7.8 Mm, suggesting that four oscillation nodes would be seen across a typical umbra. Other work (Rice and Gaizauskas, 1973) suggests that the oscillations inside sunspot umbrae are indistinguishable from the quiet-sun p-modes.

The photospheric umbral oscillations are assumed to be a passive passive response of the sunspot umbra to the driving force of the quiet-sun p-modes (Thomas 1981). The exact mechanism which couples the sunspot and the quiet Sun is unknown, and direct observational proof of this theory has not been made. An alternative scenario proposed by Moore (1973) drives the photospheric umbral oscillations with an oscillatory convection at subphotospheric levels. The coupling mechanism between the convection and the photospheric motions remains unknown and no clear observational proof of this proposal exists.

Umbral oscillations in the chromosphere are quite different from the photospheric umbral oscillations. Lites (1992) reviews many details of these oscillations; but here I review just a few relevant properties. The dominant frequency band of these oscillations is about 5 mHz, corresponding to a three minute oscillation period. The amplitude of the oscillations is large (1 to 10 km s^{-1}) and the steep waveforms often have nonlinear properties. The spatial dimension of these oscillations are much smaller than the photospheric oscillations; Lites quotes a characteristic size of 2.5 Mm. Recent observations (Shine, et al. 1991) seem to show that there are independent centers of oscillatory power in the umbral chromosphere and other observations show that waves originate from specific centers, spread across the umbra, and then induce running penumbral oscillations in the penumbral chromosphere (Alissandrakis, Georgakilas, and Dialetis 1992).

An important feature in the chromospheric spectrum is the lack of oscillatory power in the five-minute band. Similarly, oscillatory power in the photosphere with three minute periods is rare. Thus the coupling between these oscillations at two heights in the sunspot umbra remains unclear (see Campos 1989). Either the coupling is non-linear and involves a shifting of the oscillatory power in frequency, or perhaps the respective oscillatory amplitudes are too low to be detected by modern observations. Theories which explain the chromospheric oscillation spectrum employ trapping of waves in a chromospheric cavity (Zugzda, Locans and Staude, 1983) or only partial reflection of waves from temperature gradients in the umbral chromosphere and transition region (Gurman and Leibacher 1984).

1.2. Penumbral Oscillations

The only observations which might reflect oscillations in the penumbral photosphere are from Shine et al (1987). The authors observe "dark clouds" in the photospheric penumbra, having sizes larger than the width of the dark penumbral filaments. They speculate from the outward propagation of these clouds that the features are related to the chromospheric oscillations seen in the penumbra, which also propagate outward through the penumbra.

The chromospheric penumbral oscillations are oscillations which propagate radially outward through the penumbra in the direction of the Evershed flow at phase speeds of between 10 and 20 km s^{-1} (Lites 1992). The period reported by recent work from Shine, et al. (1991) is 250 s with no power at higher frequencies; this is a slightly lower frequency than the characteristic frequency of the umbral chromospheric oscillations. However these authors observe a matching of the wavefronts in the inner penumbra with umbral chromospheric oscillations, consistent with the results of Alissandrakis et al. (1992).

1.3. Quiet Sun Photospheric Oscillations

The quiet-sun p-modes represent the resonant modes of a global acoustic cavity. The interaction of these global oscillation modes with sunspots was uncovered by the work of Braun et al. (1987). In this work the authors measure an absorption of the acoustic energy of the global p-modes by a sunspot. They show that the absorption has a dependence on the spatial wavenumber of the incident p-mode such that acous-

tic waves with a wavenumber k less than about k=0.3 rad Mm^{-1} are not effectively absorbed, whereas waves with higher wavenumber k=0.8 rad Mm^{-1} are absorbed by 50%. In subsequent work (Braun and Duvall, 1990) the authors have shown that the p-mode absorption is not linearly related to the size of the sunspot and that magnetic fields associated with plage and the active region network also act as true sinks for acoustic energy (Braun et al. 1988). Recently Braun et al. (1992) have measured the scattering phase shifts of the p-modes interacting with a sunspot, as well as a temporal frequency dependence of the acoustic absorption. The interaction of global p-modes with the magnetic fields of active regions on the Sun proves to be a fertile research topic; recent discoveries show that active regions are surrounded by regions with excess high-frequency oscillation power and that subsurface magnetic fields may have a signature in the local oscillation power in the global p-modes (Braun, Lindsey, and Fan, 1992).

2. What is the Source of the Five-minute Period Umbral Oscillations?

The velocity oscillations observed in sunspots show a variety of properties. Understanding the interactions between all these oscillations in different regions of the sunspots, and the interaction of the oscillatory fields and the quasi-stationary velocity flows represents a tremendous challenge. Deciphering the physical structure of the sunspot at unobservably small scales or below the solar surface from clues offered by this rich spectrum of oscillations is another complicated task, but such studies are essential and will be rewarding. In this vein I propose a detailed observational study aimed at understanding one of the many types of oscillations seen in sunspots. I

propose to study the spatial and temporal properties of the five-minute period umbral oscillations to determine what drives them. The specific question I wish to answer is the following: are the five-minute period umbral oscillations driven by a source external to the sunspot, namely the quiet-sun global p-modes? In this final section I discuss the observational strategy for this study, and applications of the oscillations as probes of the sunspot.

2.1. Observations of Sunspots

In order to study the velocity field inside sunspots a two-dimensional map of the velocity measured from Doppler shifts of spectral features must be produced. The instruments at Mees Solar Observatory include a high dispersion spectrograph, and with the development of the Mees CCD (MCCD) Imaging Spectrograph system for this instrument it was clear that such an oscillation data set could be collected using the technique of imaging slit spectroscopy. This method is very susceptible to image motion and distortion from atmospheric seeing; specific features of the MCCD and the observational study address these susceptibilities.

2.1.1. Seeing Effects

Since the sunspot is a region with large intensity gradients, stray light (light scattered from bright regions into darker regions) is a major problem. Stray light has two sources: (1) scattered light from the imperfect telescope optics, and (2) atmospheric disturbances which defocus the image and thus mix light from different spatial regions. The telescope which feeds the MCCD instrument is a coronagraph, so scat-

tered light from the main telescope optics is insignificant, although certainly the numerous fold mirrors in the optical path do contribute a some amount of scattered light. Removing atmospheric sources of stray light is beyond the capability of the MCCD instrument. During moments of good seeing these atmospheric sources can be insignificant; but periods of good seeing are generally not long-lived, and oscillation studies mandate continuous observations for extended periods of time. Some observational technique must be used to eliminate or reduce the unwanted contamination of the data by stray light.

2.1.2. Molecular Spectra of Sunspots

Because sunspots are cool they have spectra similar to spectral type dK0 with a rich molecular spectrum (Bray and Loughhead 1964). These absorption lines are strictly confined to the cool regions of the umbra and do not appear in the photosphere. In this study I plan to measure the Doppler shift of molecular lines in order to remove contamination from stray light due to seeing.

Photospheric absorption lines are strongly affected by stray light; stray light will add a spurious line profile (the profile from the piece of oscillating photosphere) into the umbral spectra. Since the photospheric oscillation velocities are much stronger than the umbral velocities, the scattered photospheric velocity will overwhelm the umbral velocity and the data will measure some combination of velocities from umbra and the quiet Sun rather than from just the umbral plasma. The situation is much different with molecular absorption lines. Stray light will evenly fill in the molecular absorption profile with a constant intensity from the continuum. By measuring the

Doppler shift of these lines the effects of stray light can be removed; stray light will not contaminate the Doppler signal with spurious velocities, it will just make the Doppler shift more difficult to measure.

It would be useful to obtain many measurements of the umbral velocity simultaneously, and average these measurements to attain a higher signal to noise ratio. (The ratio is improved as the square root of the number of independent measurements.) The study I propose will measure the velocity from more than a dozen molecular lines simultaneously.

2.2. Using Oscillation Data to Understand Sunspots

The use of oscillation data to study structures on the Sun, particularly structures below the visible surface of the Sun is known as solar seismology. Thomas et al. (1982) proposed the idea of probing the subsurface structure of sunspots by using the velocity oscillations observed in sunspots; this concept is known as sunspot seismology. Most work in this field has attempted to fit the observed oscillation amplitudes and frequencies with various models for the physical characteristics of sunspots. Using a simple sunspot model, Abdelatif (1985) solves the problem of transmission of an acoustic wave from an unmagnetized region into a region containing a magnetic field. Results from his model shows that sunspots act as selective filters through partial transmission and reflections, allowing waves with only certain spatial wavenumber to penetrate the model sunspot. By solving for the frequency dependence of this model (see Figure 1.01) I show that not only are there specific spatial frequencies that are favorably transmitted, but also certain temporal frequencies are more favorably

transmitted into a sunspot. In general it is easier to find the temporal frequency transmission function rather than the spatial wavenumber transmission, since in oscillations observations temporal frequencies can be accurately measured. By measuring this frequency transmission function and using the results of Abdelatif we have a method to measure physical quantities such as the magnetic field and gas pressures inside the spot. Detailed analysis measuring the transmission of different wavenumbers could also reveal variations of these physical quantities with depth in the spot.

With the recent measurement of phase shifts in the quiet-sun oscillations scattered by a sunspot, the prospect for solving the inverse problem (determining the sunspot structure directly from the data) have brightened. In order to use the oscillations observed inside sunspots to solve the inverse problem much better data is needed.

3. Summary

The umbrae and penumbrae of sunspots have complex quasi-stationary flow fields, and superposed on these velocity fields are oscillatory velocities with a variety of temporal and spatial frequencies. From this set of oscillations I choose the five-minute period umbral oscillations for an observational study. Specifically these observations seek to measure whether the quiet-sun global p-modes excite the five-minute period photospheric umbral oscillations. In order to avoid problems caused by stray light I will observe the Doppler shift of molecular lines, averaging the velocity measurements from many lines to lower the noise in the measurement. This oscillation data will be useful to constrain models of sunspot structure.

References

Abdelatif, T.E. : 1985, *Umbral Oscillations as a Probe of Sunspot Structure,* Ph. D. dissertation, Univ. of Rochester.

Abdelatif, T.E., Lites, B.W. and Thomas, J.H. : 1986, *Astrophys. J* **311** , 1015.

Alamanni, N., Cavallini, F., Ceppatelli, G., and Righini, A. : 1990, *Astron. Astrophys.* **228** , 517.

Alissandrakis, C.E., Georgakilas, A.A., and Dialetis, D. : 1992, *Solar Physics* **138** , 93.

Balthasar, H., Fangmeier, E., Kuveler, G. and Wiehr, E. : 1988 in *Advances in Helio- and Asteroseismology* eds J. Christensen-Dalsgaard and S. Frandsen (I.A.U. Symp. no. 123), 183.

Beckers, J.M., Schultz, R.B. : 1972, *Solar Physics* **27** , 61.

Bhatnagar, A., Livingston, W.C., and Harvey, J.W. : 1972, *Solar Physics* **27** , 80.

Bogdan, B.W.: 1992, in *The Theory of Sunspots* , ed J.H. Thomas and N.O. Weiss, in press.

Braun, D.C., Duvall, T.L., LaBonte, B.J. : 1987, *Astrophys J.* **319** , L27.

Braun, D.C., Duvall, T.L., LaBonte, B.J. : 1988, *Astrophys J.* **335** , 1015.

Braun, D.C., Duvall, T.L. : 1990, *Solar Physics* **129** , 83.

Braun, D.C., Duvall, T.L., LaBonte, B.J., Jefferies, S.M., Harvey, J.W. and Pomerantz, M.A. : 1992, *Astrophys J.* **391** , L113.

Braun, D.C., Lindsey, C. and Fan, Y. : 1992, *Astrophy J.* submitted.

Bray, R.J., and Loughhead, R.E. : 1964, *Sunspots* (Dover Publications, Inc., New

York)

Campos, L.M.B.C. : 1989 *Mon. Not. Roy. Astro. Soc.* **241** , 215.

Garcia de la Rosa, J.I. : 1986, *The Role of Fine Scale Magnetic Fields on the Structure of the Solar Atmosphere,* eds. E.H. Schroter, M. Vazquez, A.A. Wyller, (Cambridge Univ. Press, Cambridge)

Gurman, J.B. and Leibacher, J.W. : 1984 *Astrophys. J.* **283** , 859.

Kobanov, N.I. : 1990, *Solar Physics* **125** , 25.

Leighton, R.B., Noyes, R.W., and Simon, G.W. : 1962, *Astrophys. J.* **135** , 474.

Lites, B.W.: 1992, in *The Theory of Sunspots* , ed J.H. Thomas and N.O. Weiss, in press.

Livingston, W. and Mahaffey, C. : 1981, in *The Physics of Sunspots,* eds L.E. Cram and J.H. Thomas (Sunspot, NM: National Solar Observatory), 312.

Moore, R.L. : 1973, *Solar Physics* **30** , 403.

Moore, R.L. : 1981, *Space Sci. Rev.* **28** , 387.

Moore, R.L. and Rabin, D. : 1985, *Ann. Rev. Astron. Astrophys.* **23** , 239.

Rice, J.B. and Gaizauskas, V. : 1973, *Solar Physics* **32** , 421.

Soltau, D. and Wiehr, E. : 1984 *Astron. Astrophys.* **141** , 159.

Shine, R.A., Title, A.M., Tarbell, T.D. and the SOUP Team : 1987, *Theoretical Problems in High Resolution Solar Physics II.* eds. G. Athay and D.S. Spicer, NASA Conference Publications (NASA CP-2483), 133.

Shine, R., Tarbell, T., Title, A., Topka, K., Frank, Z., Smith, K., : 1991, *Bull. Amer. Astron. Soc.* **23** no. 2, 1033.

Thomas, J.H. : 1981, *The Physics of Sunspots,* eds L.E. Cram and J.H. Thomas (Sunspot, NM: National Solar Observatory), 345.

Thomas, J.H., Cram, L.E., and Nye, A.H. : 1982, *Nature* **297** , 485.

Wiehr, E., Balthasar, H., and Stellmacher, G. : 1988 in *Seismology of the Sun and Sun-like Stars,* ed E.J. Rolfe (ESA Publications Division, Noordwijik), 269.

Zugzda, Y.D., Locans, V. and Staude, J. : 1983 *Solar Physics,* **82** , 369.

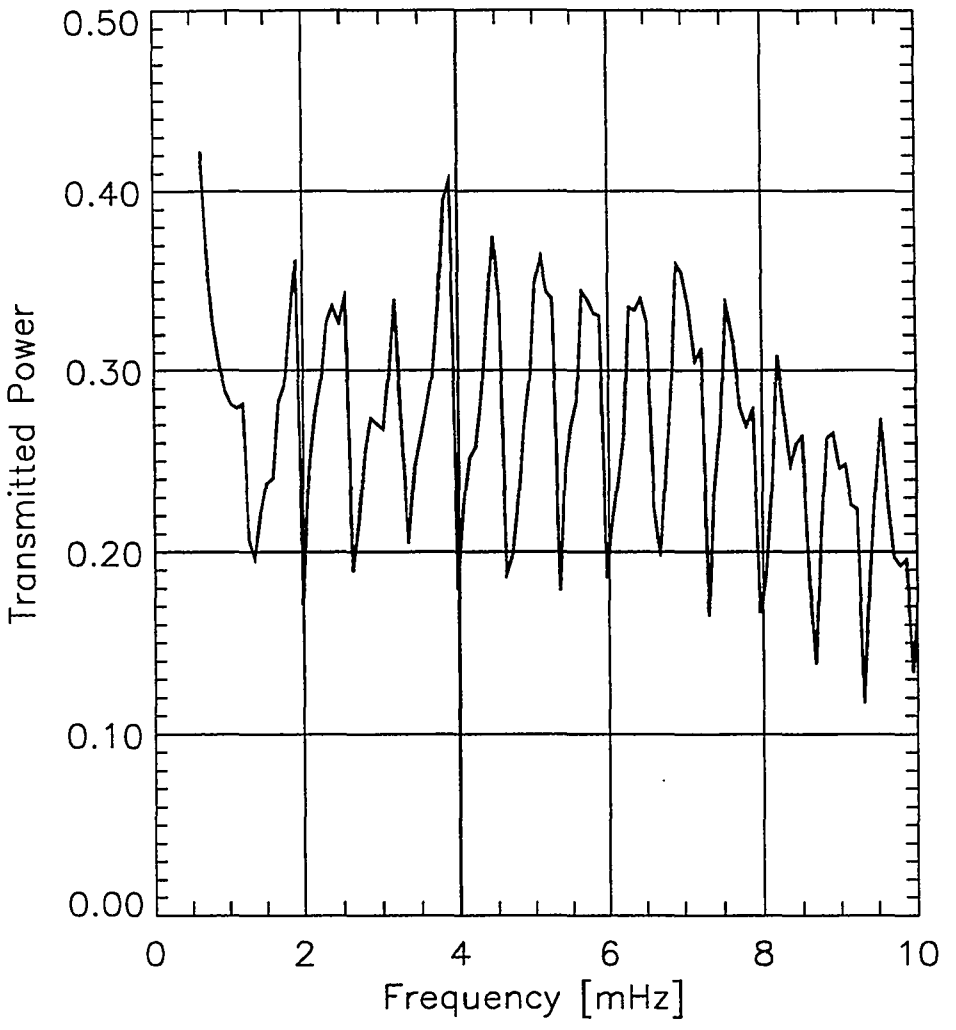

Figure 1.01 Theoretical Sunspot Acoustic Transmission Spectrum. Theoretical sunspot acoustic transmission spectrum as calculated from work done by Abdelatif 1985.

CHAPTER 2

The Mees CCD Imaging Spectrograph

Abstract

The Mees CCD (MCCD) instrument is an imaging spectroscopy device which uses the 25 cm coronagraph telescope and the 3.0 m coude spectrograph at Mees Solar Observatory (MSO) on Haleakala, Maui. The instrument works with resolving power up to $R \approx 200{,}000$ with significant throughput from λ3934 Å (Ca II K) to $\lambda \approx 10000$ Å. A fast guiding active mirror stabilizes the image during observations. A rapidly writing magnetic tape storage system allows observations to be recorded at 256 kbytes s^{-1}. Currently, the MCCD is used for imaging spectroscopy of solar flares at λ6563 Å (Hα), and velocity measurements of umbral oscillations; future plans include emission line studies of active region coronae, and photospheric studies of solar oscillations.

1. Introduction

The scientific goals of the MCCD are varied, and range from observing the slow evolution of active region coronae to providing spectroscopic diagnostics during rapid chromospheric flares. At peak performance, over a 10 hour observing day, the MCCD was intended to make 30 ms exposures, each with 0.6 arcsec spatial resolution, and 14 mÅ spectral resolution. These goals placed new demands on the image

quality, system throughput, spatial and spectral stability of the coronagraph and spectrograph instrument package.

The coronagraph and spectrograph instruments have been used in many ways since their installation in 1970. Photographic coronal work was done with these instruments (Fisher, 1971a, Fisher, 1971b, Fisher and Pope, 1971, McCabe, 1973) which was aimed at understanding the spatial and velocity distribution of coronal plasma as observed in several different spectral lines. Various spectrophotometric observations were made with the intention of studying the physical properties of prominences, (Landman, 1976, Landman, *et. al.,* 1977, Landman, *et. al.,* 1978, Landman, 1981b, Landman, 1985, Brickhouse and Landman, 1987) and solar plage (Landman, 1981a, LaBonte, 1986a, LaBonte, 1986b). Photospheric and chromospheric solar oscillations were investigated in two projects, with time series observations of the solar spectrum around C I λ5380 Å (Lindsey and Landman, 1980) and He D3 λ5876 Å (Landman, 1981a). These projects encompass most of the observations made with the coronagraph and spectrograph instrument package.

Although these instruments have been used for many years, there is no comprehensive reference which describes them. For this reason, we review the 25 cm coronagraph telescope and 3.0 m coudé spectrograph system in section 2. We describe, in section 3, the characterization of the instrument package, and the adjustments made to meet MCCD requirements. In sections 4 and 5, we explain the optical and electronic systems that comprise the MCCD instrument. We discuss two current observing programs run with the MCCD in section 6, and lastly, in section 7, we list

several future observing programs, and discuss potential uses for the MCCD instrument in solar astronomy.

2. The Coronograph-Spectrograph Instruments from 1969 to 1987

The 25 cm coronagraph telescope and 3.0 m coude spectrograph instrument package was built by Boller and Chivens in 1967. The installation of the telescope on the 3.7 m solar spar, and the spectrograph in the coude room of MSO was completed in 1970. In this section, we describe the design and features of each of these instruments prior to the MCCD project.

The coronagraph telescope (see Figure 2.01) employs a singlet 25 cm diameter, 355 cm focal length objective lens (L1). At the prime focus of this lens is a two-turret collection of occulting disks, which can occult any section of the solar limb. Light from the photosphere is reflected off these occulting disks and out of the telescope when the solar corona is being observed. A field lens (L2) following the prime focus forms a pupil image on a second objective lens (L3). Two fold mirrors (M1 and M2) fold the beam towards the center of the spar mount. The second objective (L3) is a hyperchromatic lens, and corrects for the chromatic aberration of the coronagraph lenses. After the L3, the beam reflects off a steerable coude mirror (M3) to an image plane on the slit of the spectrograph in the coude room. The image scale is 27 arcsec mm^{-1}. Just before the image plane, a three mirror image rotator (M4 through M6), directly driven by the spar removes image rotation at the coude focus.

The 3.0 m focal length coude spectrograph (see Figure 2.02) receives a solar image from the coronagraph at the slit jaw assembly. The slit jaws adjust from a width 10 μm up to several hundreds of μm. A flat folding mirror (M13) redirects the light to the collimating mirror (M14), which illuminates the diffraction grating with a collimated beam. One of two diffracting gratings disperse the light. The normal incidence grating (#1), ruled at 600 lines mm^{-1}, is blazed for use in first order with a focal plane reciprocal dispersion of 5.7 Å mm^{-1}. The echelle grating (#2) is ruled at 300 lines mm^{-1}, blazed for a $63^{o}26'$ angle of incidence, and provides reciprocal dispersions greater than 0.6 Å mm^{-1}. The camera mirror (M15) focuses the dispersed light on a curved focal plane, measuring 2.5 cm across the dispersion and 40 cm along the dispersion. Here, a 35 mm film transport can photographically record part or all of the solar spectrum. A small flat mirror (M16) directs the light to a viewport. An optional double pass beam provides greater spectral purity and dispersion.

3. Telescope Performance and Subsequent Adjustments

We made measurements of sunspots with the MCCD instrument, and characterized the slow spatial image drift. This drift was determined to have two possible sources, either (1) spurious image rotation which would introduce translational motion after the image rotator, or (2) motion of optical elements in the light beam. In order to eliminate spurious image rotation, we adjusted the pointing of the spar polar axis (see Appendix A), internally aligned the image rotator, and re-positioned the image rotator in the coude beam. Currently, the spar polar axis is measured to be within 60 arcsec of the pole, which introduces less than one arcsec $hour^{-1}$ of spurious motion in

the image plane. The image rotator was realigned using a standard technique (Kingslake, 1983), and measurements of the optical axis of the telescope made with the image rotator in the beam show that the maximum spurious translational motion introduced by the rotator is now less than 2 arcsec $hour^{-1}$. Two optical elements were found to be contributing to image motion. First, the coronagraph objective (L1) was discovered to be loose in its mounting cell, accounting for an anomalous image shift each day near local noon. Also, the mounting bracket for the coude mirror (M3) was found to be improperly balanced, and thus not properly correcting for the spar's declination motion. Currently, spurious image motion seen in the image plane is a few arcsec $hour^{-1}$, which probably results from residual imbalances in the coude mirror mount. This image motion is within the limits imposed by the MCCD design, and is completely removed by the fast guiding system.

From observations made in the steep wings of strong spectral lines, we found that the spectrograph had high frequency shaking problems, between frequencies of 1 to 3 s^{-1}. We investigated the shaking more precisely by finding shifts in a time series of zeroth order slit jaw images produced by the flat field lamp. Almost all of the high frequency shaking was eliminated when a refrigerating unit in the coude room and the air conditioning ducts of the building were mechanically isolated from the spectrograph. Low frequency drift still exists in the spectrograph with a linear slope of 15 mÅ $hour^{-1}$, and Fourier analysis shows that its amplitude decreases smoothly with frequency, containing no resonances.

Two characterizations of the final operating MCCD system are shown in Figure 2.03 and Figure 2.04; the spectrograph beam profile, and the system spectral response respectively. The spectrograph beam profile shows that the spectral point spread function has a full width at half-max (FWHM) of 28 mÅ, which is near the diffraction limit of the spectrograph. The useful spectral range of the instrument extends from Ca II K λ3934 Å to λ10000 Å, although it is possible to access regions both with wavelengths longer and shorter than this range.

4. MCCD Modifications I -- The Optical Bench

The five major revisions to the optical system of the coronagraph spectrograph required for the MCCD project consisted of: (1) providing rapid, controlled exposures, (2) scanning the solar image on the spectrograph slit, (3) producing a live video image of the solar region being studied with the spectrograph, (4) stabilizing the image with a fast guiding system, and (5) providing calibration flat field images. The MCCD optical bench (shown in Figure 2.05) has 4 beams which fulfill these requirements. The main optical beam uses a shutter mirror and an image scanning mirror to make exposures and scan the solar image. The image monitor beam produces a live video image comparable to a slit jaw image. The fast guider beam provides a motion feedback signal used to stabilize the image, and finally, the flat field beam provides calibration source for the MCCD detectors.

The main optical beam of the optical table consists of five flat mirrors (M7 - M11) and four Nikkor telephoto lenses (L4 - L7). This beam forms two pupil images, one on the active mirror (M9), and the other near the fast shutter (M10) and

image scanning (M11) mirrors. The two associated image planes are located just before M8, and between L5 and L6. The shutter mirror (M10) is a flat mirror mounted on a galvanometer motor. When closed, the shutter mirror sends light into the image monitor bench, while open (removed from the beam) it allows light to pass to the scanner mirror and eventually to the spectrograph. The shutter motion is linear and stable down to exposures of 25 ms. The scanning mirror (M11) is used to scan the solar image across the spectrograph slit. This mirror is also mounted on a galvanometer motor, and can scan the entire field of view (several hundred arcsec) across the spectrograph slit in a few ms.

The image monitor beam of the optical table produces a live video display of the solar region observed by the spectrograph. The beam from the closed shutter mirror is re-imaged by a 50 mm Nikkor lens (L8) and enlarged to an appropriate image scale via a 75 mm Nikkor lens (L9). By repositioning this lens (L9) and the detector (C2), a range of image scales can be produced. A pentaprism (P) flips the image left to right to achieve the desired N-S-E-W image orientation, and various interference filters (F) can be positioned in the beam to isolate different wavelengths. The image plane detector (C2) for this beam is a Cohu video rate CCD camera.

A thin glass plate acts as a beam splitter (BS) and directs light out of the main beam into the fast guider beam. A section of the solar surface is selected by tilting the beam splitter. The zoom lens (L11) allows a variable image scale to be formed on the pointing camera (C3) and the position sensor (PS). Motion of a high contrast feature, such as a sunspot, on the position sensor produces an analog translational

error signal, and the zooming capability of the beam allows this signal to be optimized by changing the size of the high contrast feature. The error signal is used through a feedback system to rapidly adjust the tilt of the active mirror (M9), to eliminate image motion at all points downstream of M9. The technique of making spectroheliograms with a slit spectrograph is sensitive to image motion, and the improvement from use of the fast guider system is shown in Figure 2.06. The fast guider has another feedback loop to the coude mirror (M3) of the coronagraph telescope, which enables the system to follow features as they rotate across the solar disk.

The final function of the MCCD optical bench is to produce calibration flat field images. The integrating sphere (IS) isotropically scatters light from a tungsten filament source into all solid angles. A translation stage moves a field lens (L12) into the position of the first fold mirror (M7). The lens images the exit port of the integrating sphere at the first solar image near M8. This allows the calibration beam to transit the optical table in exactly the same manner as the beam from the coronagraph. The flat fielding system provides a flat spatial image, and a smoothly varying black-body spectral profile.

5. MCCD Modifications II -- Detectors and Control Systems

At the spectrograph image plane is a Photometrics CCD camera, (C1) a Thompson UV enhancement coated 384 x 576 pixel device. Each pixel is 22 μm on a side, which corresponds to a 0.6 arcsec pixel^{-1} spatial scale. This signal is digitized to 12 bits upon readout, and the device is capable of on-chip binning. The CCD was measured to digitize 30 photoelectrons (pe) per analog-to-digital unit (ADU), with a

readout noise of 41 pe. The measured dark current for the device is linear at 0.5 ADU s^{-1}. The CCD device is cooled to -42 C with a thermo-electric system.

The image monitor bench uses a Cohu 6410 video rate CCD camera as a detector. The camera has 774 x 242 pixels, each sized 8.5 x 19.75 μm. This CCD uses frame transfer to readout the detector at video rates, and an electronic shutter allows exposure times of 0.5, 1.0 and 33 ms. This camera is not cooled.

The control system for the MCCD is run with a 68020 based Ironics Performer 32 single board microprocessor VME system. Mounted on the VME bus are several auxiliary boards. The processor communicates with the Photometrics CC200 controller via a National Instruments GPIB VME board. Also on the VME bus is an Imaging Technology 640/2 frame grabber board, which receives the video signal from the image monitor bench Cohu camera control box, and digitizes it to a 640 x 480 pixel image, 1 byte deep. Several functions are performed by an Ironics VME Parallel Input/Output board, including driving the shutter and scanner mirrors, illuminating the tungsten filament, and moving the M7 - L12 translation stage. Finally, the fast guider system is interfaced with the Ironics controller via a Datem VME BitBus board and custom electronics which control the active mirror and other elements in the fast guider beam. The system contains two 8 mm Exabyte magnetic tape drives, one accessible from the Photometrics controller, the other accessible from the Ironics.

The pSOS real-time operating system, produced by Software Components Group, Inc., is used to run the MCCD. The control system for the MCCD is written with the *c* language in a UNIX environment, compiled into a pSOS executable kernel, and

then the Ironics system is rebooted using this kernel. The pSOS control software allows direct user control of simple system tasks, such as exposing the Photometrics CCD, reading the image, and storing it to magnetic tape. Several observing modes, programmed with user defined parameters, can also be run with the software.

6. Observations with the MCCD Instrument

The MCCD control software offers so many user parameters that an enormous variety of observational programs are possible using the instrument. While considerably complicating the observations, this flexibility exists to allow an observing program to be defined from scientific considerations. There are 13 adjustable parameters in the MCCD system. They are number, binning, and offset of the spatial pixels, number, binning, and offset of the spectral pixels, number and size of the scan steps, exposure time, spectrograph slit width, spectrograph grating choice, spectrograph grating angle, and spectrograph prefilter. Consider the three parameters, spectral binning, slit width, and exposure. Spectral binning can be defined from a scientific consideration; namely the spectral resolution desired in the observations. Once the spectral binning is determined, it defines an optimal value for the spectrograph slit width. However, the slit width can be adjusted over a range of values and still produce satisfactory observations. When the slit width is established, it determines the amount of light entering the spectrograph and thus the exposure time required for the observations. Flexibility in the system allows trade-offs between combinations of slit width and exposure time, which can be optimized to fit best with other scientific objectives of the observing program.

The general problem of determining the observing parameters is not this simple, since no parameters form an isolated set. (In the above example, the slit width also influences the scan step size, and the exposure time affects the overall scan repetition time, and thus the optimal scan range.) The general approach is to define as many parameters as possible from the primary science objectives of the observations. The remaining parameters are balanced with one another in order to optimize the observations for the secondary science objectives. In Table 2.1 we list observational parameters for two unique observational studies. We designed the flare study to observe rapid chromospheric flares in active regions. The primary requirement for this program is the capability to observe an active region at Hα several times each minute. Secondly, these observations must have sufficient spectral resolution and range to study the velocities found in flares, and sufficient spatial resolution to distinguish flare kernals. Unfortunately these goals work against each other, since as more pixels are used to increase the spatial and spectral resolution and range, more time is needed to read and store the data. Ultimately, trade-offs were made between the opposing goals, and the observations were configured as shown in Table 2.1. We designed the umbral study to observe sunspot umbral oscillations with high velocity sensitivity, and thus the primary requirement of this study is very high spectral resolution. The secondary goals were to observe a small region, only a sunspot umbra, and to repeat the observations once every 60 seconds, to resolve the desired acoustic oscillations. Balancing these goals and other considerations, we arrived at the observing parameters listed in Table 2.1.

The only unyielding factor in the MCCD system is the speed at which a region can be repetitively scanned. We want the time required to scan the solar image across the spectrograph slit to be as small as possible, as with all imaging spectroscopy programs using a slit spectrograph. The limits we encounter with the MCCD are of two types; limits from the continuous data storage speed, and limits from long exposure times. The time required to collect and store one frame at one slit position on the solar surface t_{frame} is given (in ms) by:

$$t_{frame} = 11.79 + 0.51\ (N_{spec}) + 0.0038\ (N_{spec})\ (N_{spat}) + 0.0126\ (B_{spec}-1) + 0.015\ (O_{spec}) + \mathrm{MAX}\ (t_{tape}, t_{expos}) \tag{1}$$

where N_{spec}, B_{spec}, and O_{spec} are the number, binning and offset values of spectral pixels in the observations, N_{spat} is the number of spatial pixels in the frame, and MAX (t_{tape}, t_{expos}) is the longer of two times, either the time required to store the frame to magnetic tape, or the frame exposure time. The time required by the MCCD to write one frame to the tape system t_{tape} is given (in ms) by:

$$t_{tape} = 20.57 + 0.0039\ (2\ N_{spat}\ N_{spec}) \tag{2}$$

In practice, the Exabyte tape storage system determines a maximum operating speed for the MCCD observations, since it is never shorter than the shortest frame exposure; the flare observations described in Table 2.1 are limited by the tape write speed. However, as shown in equation 1, when the exposure time t_{expos} exceeds the tape write time t_{tape}, the total frame time becomes controlled by the spectrograph exposure time. Such is the situation in the umbral observations described in Table 2.1.

Finally, the time required to complete a scan of the solar surface t_{scan}, is simply

$$t_{scan} = (N_{scan})\,(t_{frame}) \tag{3}$$

which is the product of the number of individual frames (N_{scan}) and the time to observe and store one frame t_{frame}.

We have used the new MCCD to make observations of solar active region flares in the Hα (λ6563 Å) spectral line. Typical flare observations examine 19 Å of the solar spectrum centered on Hα, and scan a 216 x 216 arcsec region on the solar surface with a repetition rate of 12 seconds (see Table 2.1). In Figure 2.07, we display sample flare spectra, which show a strong Hα emission excess at 2.5 Å blueward of line center, characteristic of particle precipitation in the chromosphere (Canfield, *et. al,* 1991). The imaging capability of the MCCD is used to determine the sites of particle precipitation, and the correspondence of these sites with flare kernels. We also make simultaneous measurements of the vector magnetic field with the Haleakala Stokes Polarimeter (Mickey, 1985) to compare these precipitation sites with regions of current flow (Canfield, *et al.,* 1991).

Another program using the MCCD system studies the oscillation modes in sunspot umbrae. We measure the velocity shifts of molecular absorption lines, which are produced only in the umbral region. Typical observations examine a 38 x 38 arcsec region centered on a sunspot umbra, and span 5Å of the solar spectrum, centered at λ6404 Å. In Figure 2.08, we show a sample spectrum of several molecular lines seen in a sunspot umbra, which have been identified with molecules of TiO, CaH, CN and

MgO. (Boyer, *et al.*, 1975) The mean velocity shift of four of these lines is computed, and averaged over all umbral pixels; then the spectrograph wavelength drift is subtracted via a low frequency temporal filter. Figure 2.09 shows a plot of the residual velocity signal and Figure 2.10 shows a power spectrum of this velocity. The high frequency noise power in Figure 2.10, unaffected by the temporal filter, can be used to calculate the velocity error in the averaged data. The noise corresponds to a total velocity error of 3 m s^{-1}, and a single measurement velocity error of 95 m s^{-1}.

7. Future Use of the MCCD

The Hα flare study with the MCCD is planned to run through the end of this solar cycle. Each day the program is run, many hours of imaging spectroscopy data on one active region are stored. Currently, a catalog of data is being built, and only cursory looks at the data have been made. Along with a continuing plan to compare the data with regions of current flow from vector magnetic fields, plans exist to search for proton beam signatures with the Haleakala Stokes Polarimeter, and to compare these observations with the MCCD data.

The image monitor bench of the MCCD system is being used to observe high degree p-mode intensity oscillations. We plan to correlate umbral oscillations observed spectroscopically (as in Figure 2.10) with the absorption of p-modes by sunspots, as measured with the image monitor camera. Also, a program to study high degree high frequency p-mode oscillations spectroscopically is planned.

Coronal observations in Fe XIV λ5303 Å have been made. We plan to develop this program, including observations during preceding and following the the 11 July 1991 solar eclipse. We will try to develop a program to observe the corona in several lines, in order to investigate the temperature and density distribution of coronal plasma.

The MCCD system was originally designed to operate several spectrographic CCD cameras, simultaneously observing several different spectral regions. The feasibility of such a system has been demonstrated since the current system has a wide spectral range. Such multi-line observations would have the potential to study the depth dependence of energy flux in solar flares. We would be able to directly measure the propagation of acoustic energy into the solar atmosphere. We could investigate the p-mode absorption of sunspots in the photosphere and the chromosphere simultaneously, and make simultaneous observations of coronal plasma in several emission lines to directly determine the distribution of coronal gas at many temperatures.

References

Brickhouse, N.S., Landman, D.A. : 1987, *Astrophys. J.* **313** , 463.

Boyer, R., Sotirovski, P., and Harvey, JW : 1975, *Astron. Astrophys. Suppl.* **19** , 359.

Canfield, R.C., Fan, Y., Leka, K.D., McClymont, A.N., Wuelser, J.P. : 1991, in L. November (ed.), *Solar Polarimetry* National Solar Observatory, Sunspot (in press).

Fisher, R.R. : 1971a, *Solar Physics* **19** , 431.

Fisher, R.R. : 1971b, *Solar Physics* **19** , 440.

Fisher, R.R., Pope, T. : 1971, *Solar Physics* **20** , 389.

Kingslake, R. : 1983, *Optical System Design,* 1st ed., Academic Press, Orlando

LaBonte, B.J. : 1986a, *Astrophys. J. Suppl.* **62** , 229.

LaBonte, B.J. : 1986b, *Astrophys. J. Suppl.* **62** , 241.

Landman, D.A. : 1976, *Solar Physics* **50** , 383.

Landman, D.A., Edberg, S.J., Laney, C.D. : 1977, *Astrophys. J.* **218** , 888.

Landman, D.A., Illing, R.M.E., Mongillo, M. : 1978, *Astrophys. J.* **220** , 666.

Landman, D.A. : 1981a, *Astrophys. J.* **244** , 345.

Landman, D.A. : 1981b, *Astrophys. J.* **251** , 768.

Landman, D.A. : 1985, *Astrophys. J.* **295** , 220.

Lindsey, C.A., Landman, D.A. : 1980, *Astrophys. J.* **237** , 999.

McCabe, M.K. : 1973, *Solar Physics* **30** , 439.

Mickey, D.L. : 1985, *Solar Physics* **97** , 223.

TABLE 2.1

Two Sample Observing Studies with the MCCD

MCCD Parameter	Flare Study	Umbral Study
Spatial number	90	64
Spatial binning	4	1
Spatial offset	0	0
Scan number	90	64
Scan step size	4	1
Spatial range (arcsec)	216 x 216	38 x 38
Spatial scale (arcsec pix^{-1})	2.4	0.6
Spectral number	50	384
Spectral binning	3	1
Spectral offset	0	0
Spectral range (Å)	18.75	5.48
Spectral dispersion (Å pix^{-1})	0.375	0.014
Slit width (μm)	88	60
Grating	#1	#2
Grating angle	11° 22'	59° 52'
Spectral prefilter	ND 2.0	#1004
t_{expos} (ms)	25	600
t_{tape} (ms)	55.7	212.3
t_{frame} (ms)	110.1	901.0
t_{scan} (s)	9.9	57.7

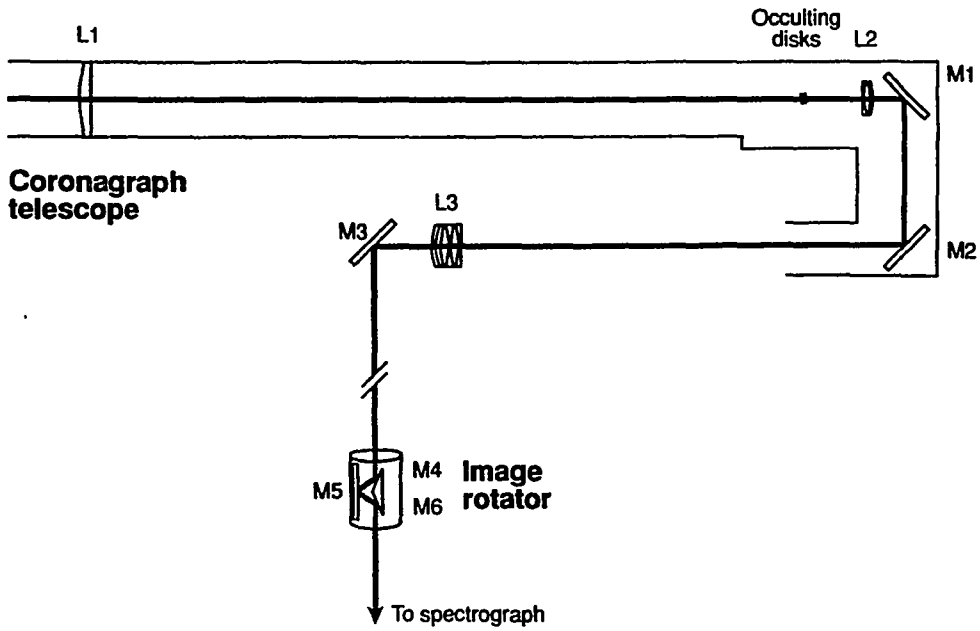

Figure 2.01 Optical diagram of the 25 cm coronagraph telescope. At the focus of the objective (L1) is a selection of occulting disks which allow the corona to be observed. The second objective (L3) corrects for the chromatic aberration of the telescope. The coude mirror (M3) directs the sunlight into the image rotator, which removes rotation from the image plane. In the current setup, the MCCD optical bench immediately follows the image rotator. (see Figure 2.05)

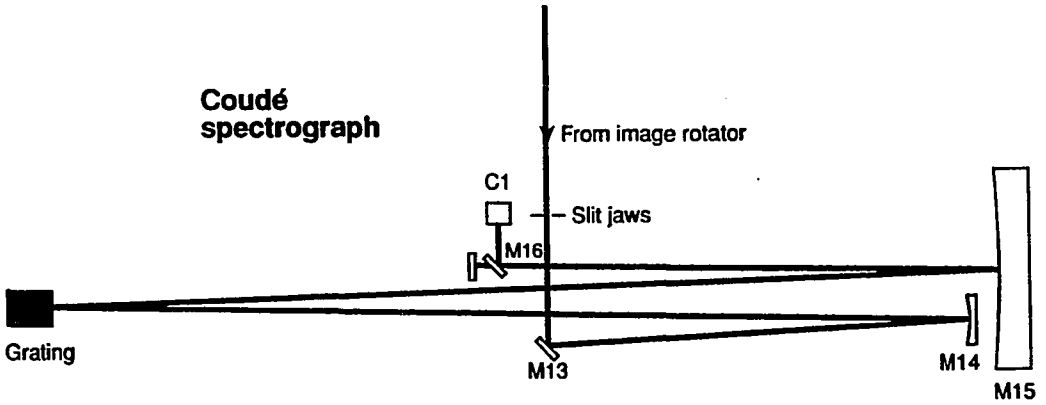

Figure 2.02 Optical diagram of the 3.0 m coude spectrograph. The slit jaws allow sunlight to enter the spectrograph, which is collimated by M14, dispersed by the diffraction grating, and focused by the camera mirror, M15. A small flat mirror (M16) feeds part of the spectrum to the Photometrics CCD camera, C1.

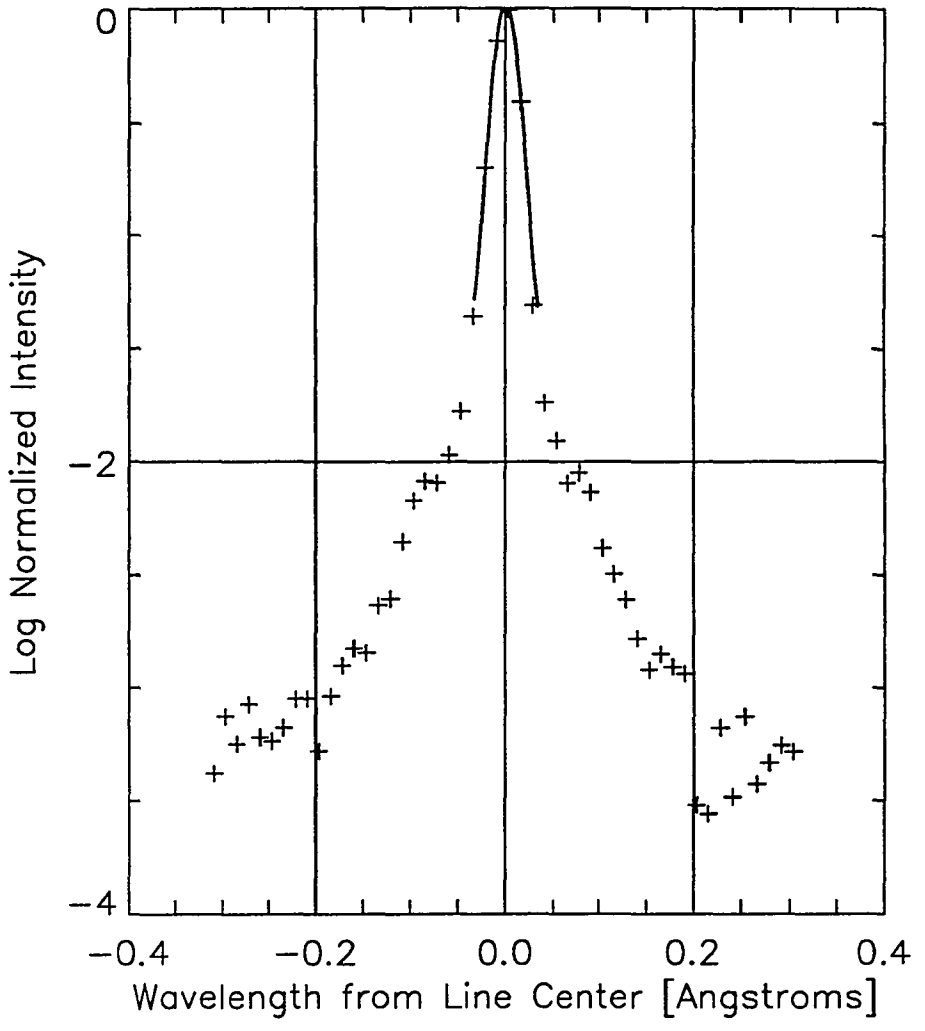

Figure 2.03 The response of the MCCD system to a HeNe laser beam at λ6328 Å. We used the echelle grating (#2) with a 42μm slit and a long exposure of 100 s. A gaussian fit to the observed line core (solid line in the figure) gives a full width at half-max (FWHM) of 28 mÅ. This implies that the spectral resolving power $R = \frac{\lambda}{\delta\lambda} = 226{,}000$.

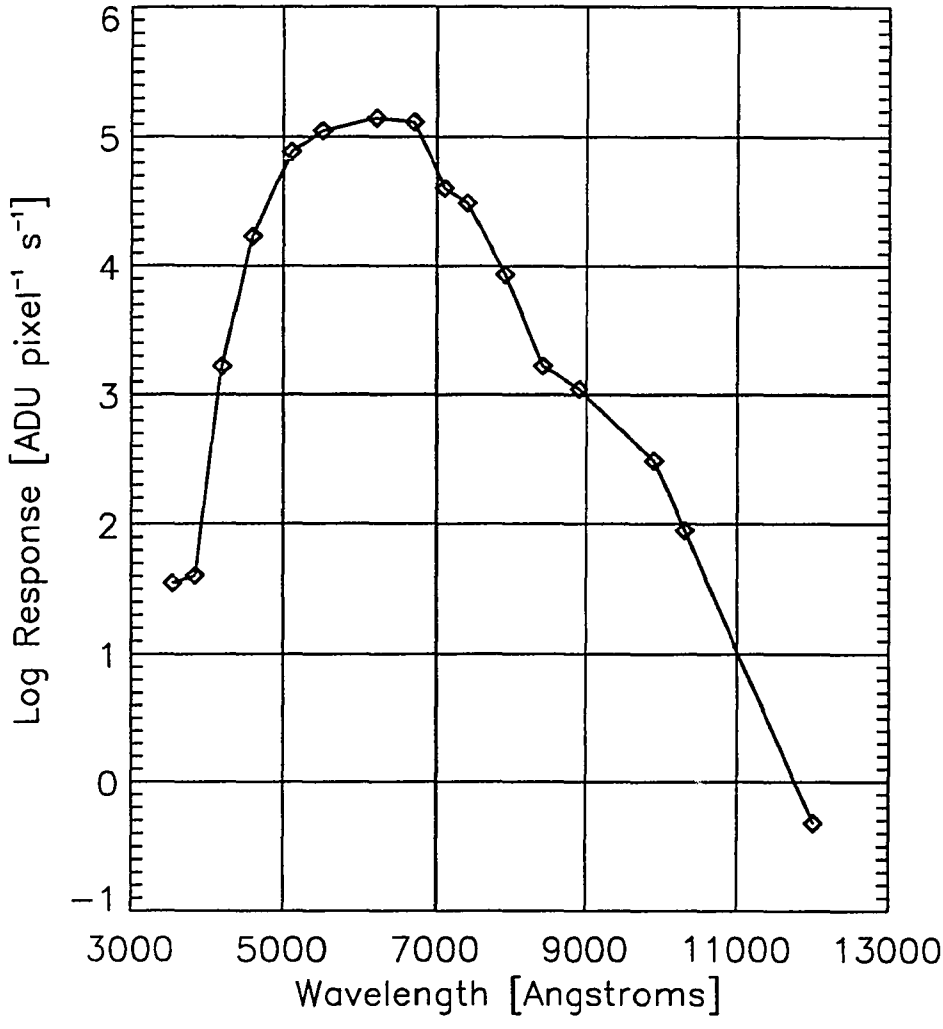

Figure 2.04 The spectral response of the MCCD from λ3550 Å to λ12000 Å This graph shows the solar flux, in ADU (analog-digital units) per second per pixel, detected by the Photometrics CCD camera at the spectrograph focus. We observed several solar continuum regions at the center of the solar disk at local noon, with the normal incidence grating (#1) (with a dispersion of 8 pixels Å^{-1}) no pre-filters, and a 60 μm wide slit. From this graph we can calculate the exposure time needed for any observation, using simple linear extrapolations to the particular observational parameters. Note that the Photometrics camera saturates all 12 bits at a value of $\log_{10}(4095) \approx 3.6$.

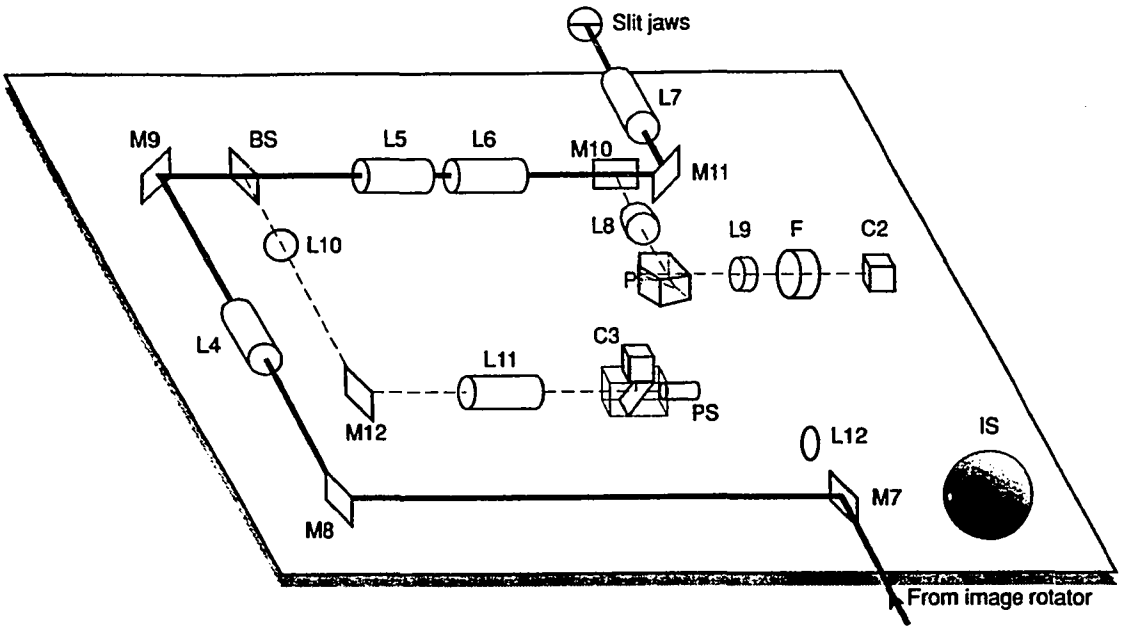

Figure 2.05 The MCCD optical bench. The image rotator directs light onto the bench at M7. The main optical beam directs light via M8, through L4 to M9, through L5 and L6 to M11, then through L7 onto the spectrograph slit. The image monitor beam takes light from the closed shutter mirror M10, through L8, the pen-taprism P, L9, and a narrow-band filter F to the camera C2. The fast guider beam directs some light via the beam splitter (BS) through L10, off M12, and through L11 to the detector package consisting of the camera C3 and the position sensor (PS). Finally, the integrating sphere (IS) and a field lens L12 produce a calibration image for flat fielding purposes.

Figure 2.06 The effect of the MCCD fast guider. These two sample spectroheliograms were taken with a spatial scale of 0.6 arcsec pixel^{-1}, a dispersion of 8 pixels Å^{-1}, with a slit width of 75 μm, and are centered on Hα, λ6563 Å. Each spectral frame (a single line in the image) was exposed for 75 ms, and then the image was stepped 0.6 arcsec perpendicular to the slit. Both images required about 180 seconds of time to compose, and were taken within 10 minutes of each other. The field of view is roughly 4 by 5 arcminutes in each frame. The direction along the spectrograph slit is horizontal, and the direction of the scan is vertical. The improvement in image quality in this case indicates that most of the image degradation arises from simple image motion, and not stretching or higher order distortions.

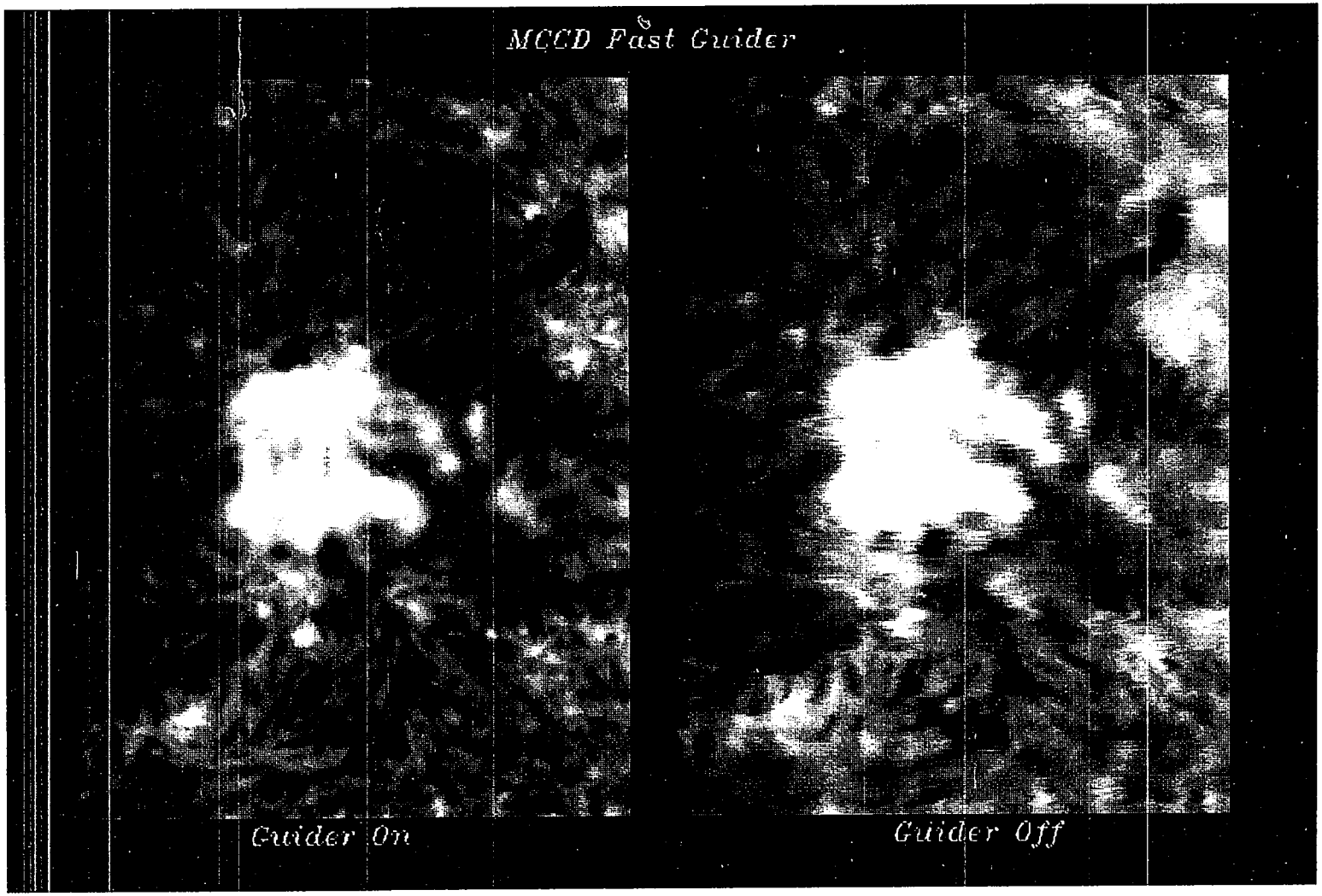
MCCD Fast Guider
Guider On
Guider Off

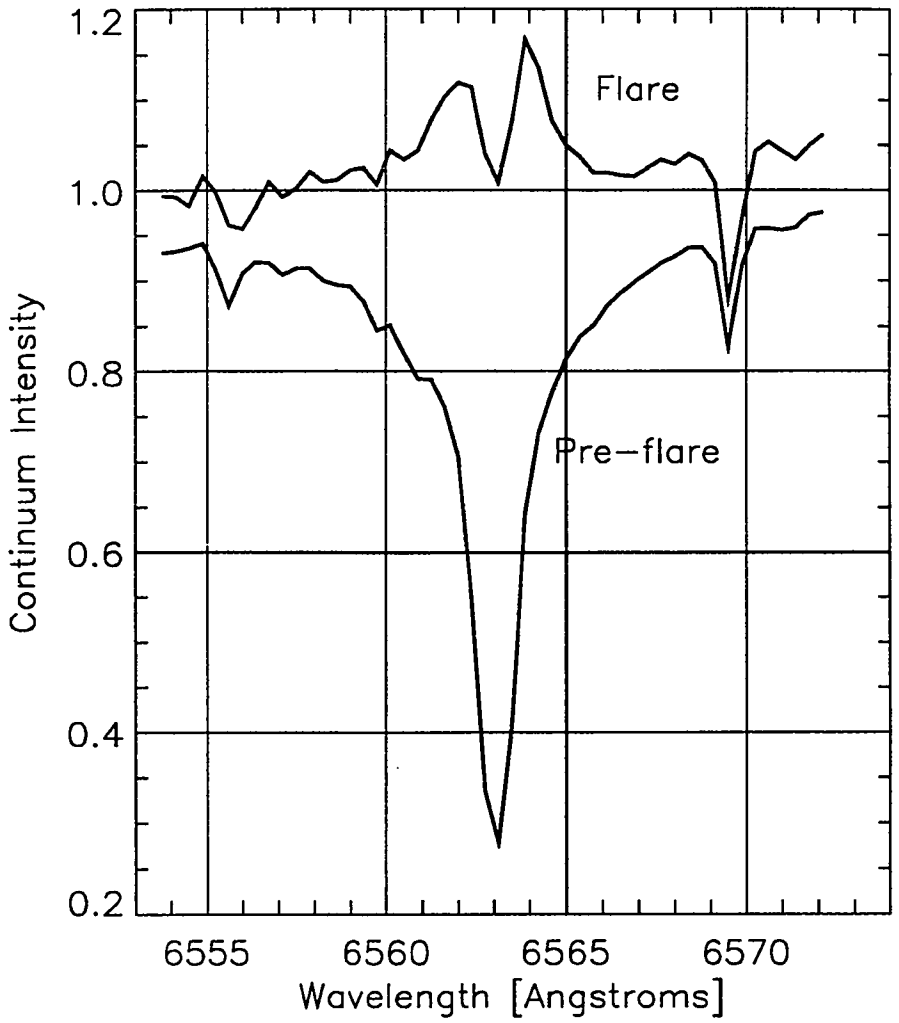

Figure 2.07 Flare observations made with the MCCD. See Table 2.1 for the observational parameters used to collect this data. In this plot we compare a quiet-sun Hα profile with a region showing excess emission during a flare. The emission profile suggests particle precipitation in the chromosphere. (Canfield, *et al.*, 1991)

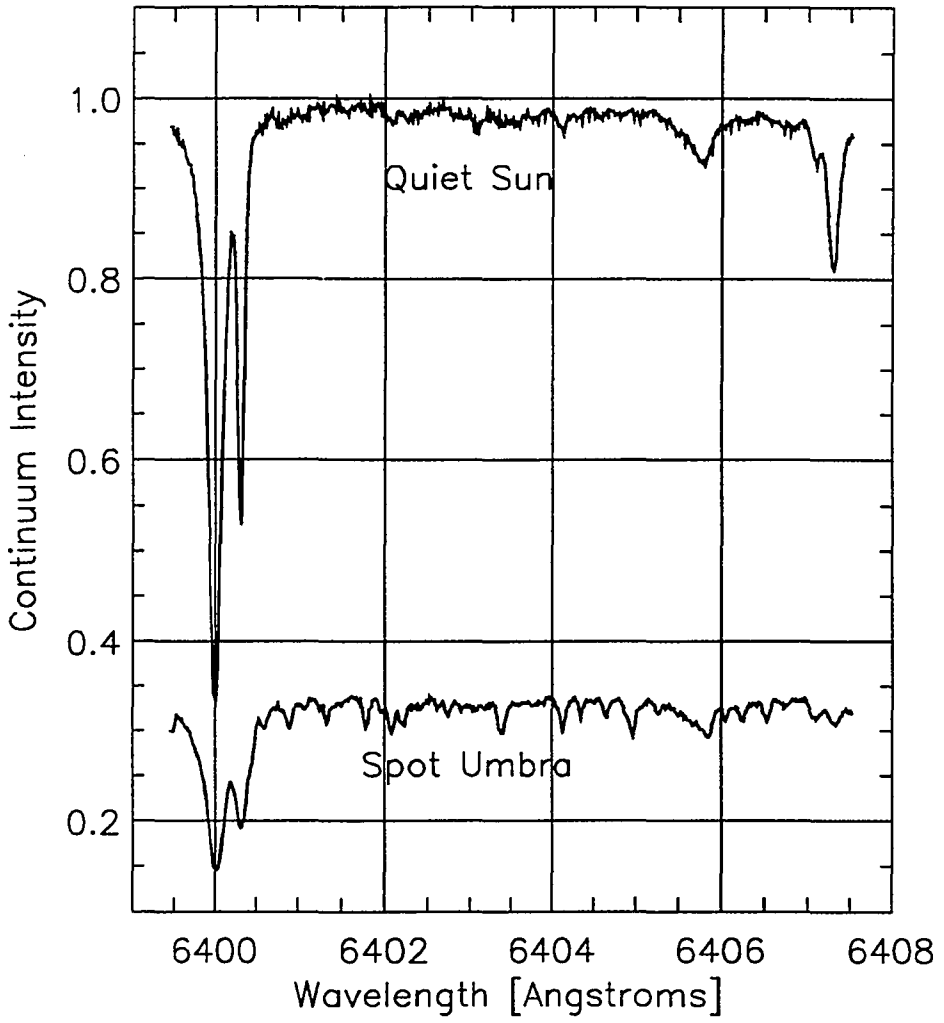

Figure 2.08 A sample spectrum of a sunspot umbra and the same spectral range of the quiet Sun, as taken with the MCCD. Visible in the umbral spectrum are several faint molecular absorption lines; the strongest four lines (λ6401.8, λ6403.4, λ6404.2, and λ6404.9) were used to measure the Doppler velocity shown in Figure 2.09

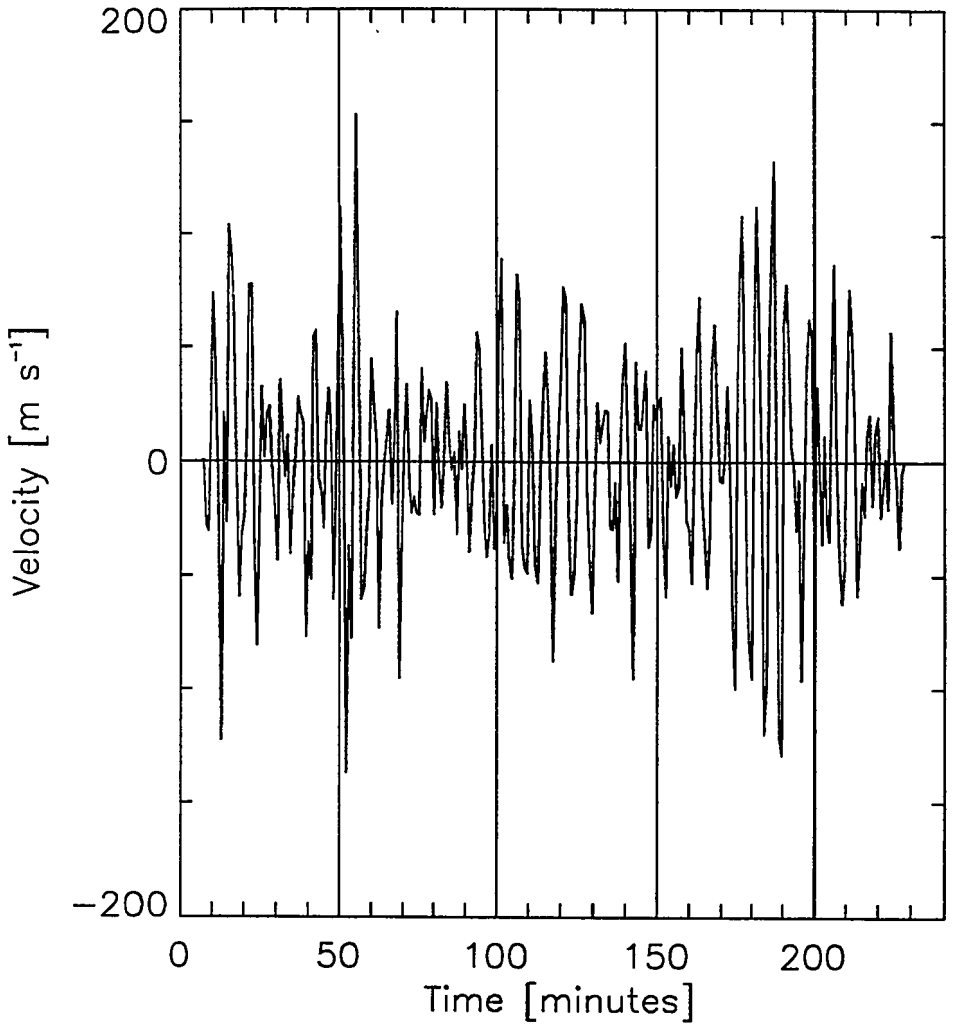

Figure 2.09 The velocity of the sunspot umbra in the main umbra of NOAA group 5836 on 15 December 1989, as determined from Doppler shifts of the molecular lines seen in Figure 2.08. The velocity is averaged over all four lines, and over the entire umbra (260 pixels); a low frequency temporal filter is used to subtract spectrograph wavelength drift from the original data, and we plot the residual velocity, corrected for line of sight. Just under four hours of observations are plotted.

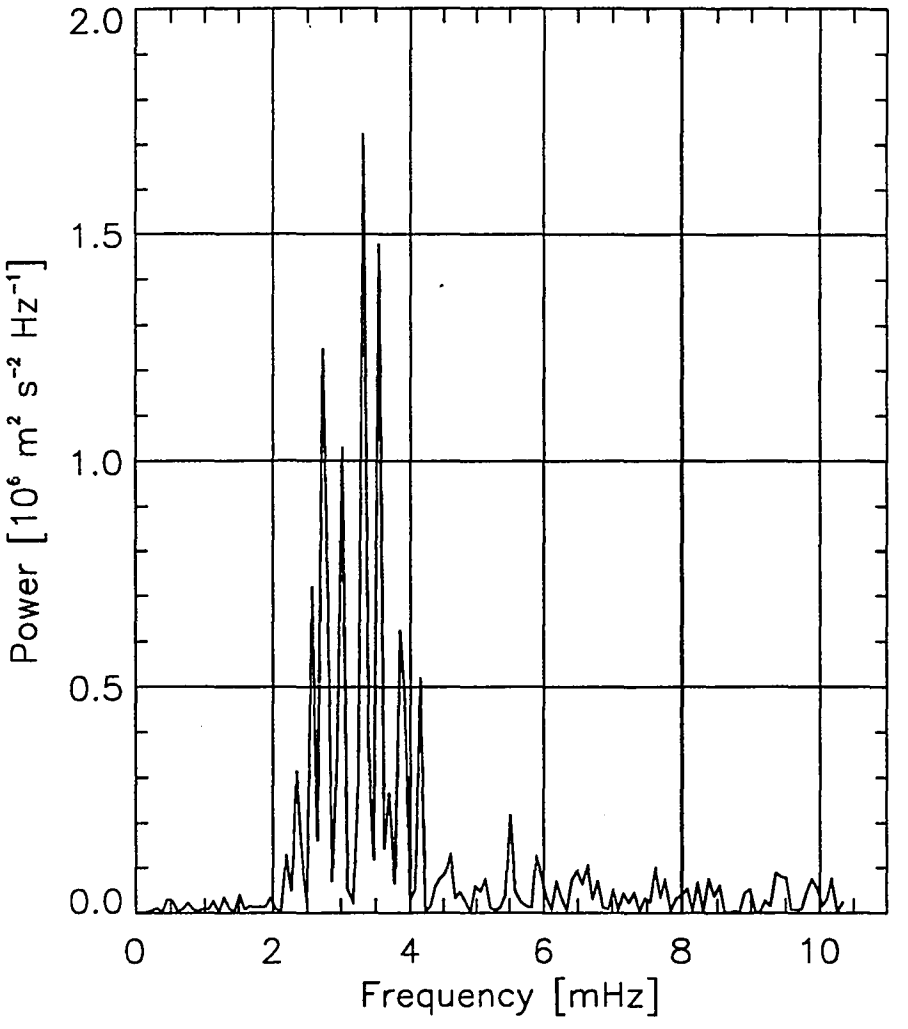

Figure 2.10 A power spectrum of the velocity signal shown in Figure 2.09 Several distinct oscillation peaks can be seen in the frequency range associated with solar p-mode oscillations. The high frequency noise power in this figure implies that the noise in the velocity signal is less than 3 m s^{-1}. Individual peaks are probably not significant.

CHAPTER 3

The Source of Five Minute Period Photospheric Umbral Oscillations

Abstract

We observed the oscillations in the umbrae of two sunspots using the MCCD imaging spectrograph at the Mees Solar Observatory (MSO) on Haleakala, Maui. We observed the Doppler shifts of 18 molecular lines in both umbrae for over 50 hours each during the interval from 11 to 16 May 1991. We find only a weak correlation between the velocity measured with molecular lines and the velocity measured using two iron lines. We remove solar rotation, image drift, and interpolate all the data onto an even time grid. We perform four spatial analyses of the umbral velocity and find (1) there is more power traveling toward the center of the umbrae than leaving the center of the umbrae (this provides a direct measure of the absorption of p-modes by the sunspot umbrae) (2) the umbral oscillations display power at the same spatial and temporal frequencies of the the quiet-sun oscillations, within the limits provided by the observations, (3) a Fourier-Bessel analysis shows no obvious resonant frequencies which might represent natural oscillation modes of the sunspot umbrae, and (4) the centers of the umbrae have less RMS velocity than the edges of the umbrae. From these analyses we conclude: (1) the photospheric umbral oscillations are driven by a source external to the sunspot, the global p-mode oscillations, (2) there are no resonant frequencies in the oscillations, which suggests there is no acoustic cavity

formed by the umbrae, and (3) the absorption of oscillatory waves is observed inside the spot, and the absorption may occur uniformly across the spot umbrae.

1. Introduction

There are several excellent reviews of the oscillatory phenomena observed in different parts of sunspots (see Moore 1981, Thomas 1985, and Lites 1992) and in Chapter 1 we discuss the relation of the photospheric umbral oscillations to other types of oscillations observed in sunspots. In this study we want to stress the following previously determined observational facts concerning photospheric umbral oscillations:

(1) **Photospheric oscillatory motions have much lower amplitudes inside sunspot umbrae than in the quiet Sun.** This was first seen in observations by Leighton, Noyes and Simon (1961); their data showed that oscillations in sunspot penumbra were relatively quiescent compared with the quiet-sun oscillations but they were unable to measure the oscillations in the sunspot umbra. Howard (1967) showed at low spatial resolution a reduction of oscillatory amplitude by 25% (corresponding to a power reduction of a factor of 2) in regions with magnetic fields compared to regions without magnetic fields. Subsequent sunspot observations with better spatial resolution and using umbral absorption lines have shown that the oscillatory power inside sunspot umbrae is reduced by perhaps as much as a factor of 20 from the oscillation power of the photosphere (Livingston and Mahaffey, 1981).

(2) **The spatial characteristics of oscillations in sunspot umbrae remain unknown.** The observations suggest conflicting results regarding the spatial nature of umbral oscillations. Observational evidence can be found implying that the umbral oscillations have spatial characteristics completely independent of (Kobanov 1990), related to (Abdelatif et al 1986), or identical to (Rice and Gaizauskas, 1973) the spatial properties of the quiet-sun oscillations.

(3) **The sunspot umbral photosphere oscillates with temporal frequencies similar to the surrounding photospheric p-mode oscillations at 3.2 mHz.** Although Beckers and Schultz (1972) concluded that the temporal frequency of oscillations inside sunspot umbrae were higher than the frequencies of the photospheric oscillations, their work used a photospheric absorption line and simply dismissed the observed five-minute period oscillations centered at 3.2 mHz as contamination from the nearby photosphere. Observations by Bhatnagar, Livingston and Harvey (1972) use the Doppler shift of three umbral absorption lines (one from the TiO molecule), a technique which excludes contamination from the stronger velocity oscillations of the surrounding photosphere; but their data still show umbral oscillations in the five-minute band. This and subsequent work has shown that photospheric umbral oscillations have a power distribution with no frequency shift relative to the power distribution of the quiet-sun photospheric oscillations.

(4) **There are no observations of well resolved umbral oscillation frequency modes.** Although some authors have tried to identify unresolved power peaks as

oscillation modes (Thomas et al. 1982, Campos 1989), the frequency positions of these peaks differ in different observations, and actually show variations within the same data set (Lites 1992). This is consistent with the assumption that the photospheric umbral oscillations have a fine scale frequency structure which is unresolved in all current observations of umbral oscillations.

(5) **There is strong interaction between sunspots and the global p-mode oscillations of the quiet Sun.** Braun et al. (1987) observed the quiet-sun oscillations in regions surrounding sunspots and concluded that sunspots absorb acoustic energy from the quiet-sun p-modes, and recently Braun et al. (1992) have measured the phase shifts from the scattering of acoustic waves in the quiet Sun from a sunspot. These observations offer only indirect evidence concerning the mechanism involved in the absorption process, but they prove there is a strong physical interaction between the quiet-sun oscillations and sunspots.

The observations used in this work were collected with the MCCD instrument (Penn, et al 1991) with the intention of producing a long time series of accurate umbral velocity measurements using pure umbral absorption lines at high spatial resolution. The data are unique in several ways. The data represent the longest time series of observations of umbral oscillations available and thus they provide better frequency resolution (by a factor of about five) than any study to date. The data simultaneously measure many umbral absorption lines; averaging the velocity computed from all of these lines reduces the measurement noise by a factor of four over previous studies. Finally by using the MCCD imaging spectrograph with its fast guiding

mirror the data maintain their spatial integrity even in the presence of less than optimal atmospheric conditions; this is essential to study the spatial structure of the oscillations.

Using this data we analyze the spatial and temporal properties of the umbral oscillations, and with this knowledge we address three questions about the physical nature of the umbral oscillations:

(1) *Is the driving source of these oscillations located inside or outside the sunspot?*

(2) *Is there an umbral acoustic cavity which produces resonances in the photospheric umbral oscillations?*

(3) *What is the physical connection between the photospheric umbral oscillations and the absorption of photospheric p-mode oscillations?*

The answers to these questions will provide insight regarding the nature of acoustic waves in sunspots and about the structure of the sunspots themselves.

The remainder of this chapter is organized in the following manner: first we review the observations and examine their inherent limitations in Section 2. We discuss the data reduction from raw spectral frames to velocity snapshots in Section 3. In Section 4 we discuss several spatial analyses used to investigate the umbral oscillations. Finally in Section 5 we review the spatial and temporal properties of the umbral oscillations and then answer the questions about the physical nature of photospheric umbral oscillations.

2. Observations of NOAA 6619 and NOAA 6625

During the set-up of the observations for NOAA 6619 on 10 May 1991, the MCCD instrument observing parameters were chosen to collect the best spectra of the umbra while keeping the scan repetition time near 90 seconds. Values for some of the final observing parameters are listed in Table 3.1. The main umbrae of active regions NOAA 6619 and NOAA 6625 (see Figure 3.01) were scanned in the observations from 11 to 16 May 1991; a set of wide field images using a broad band filter centered on the Ca II K line at λ3934Å was taken with the image monitor camera during each scanning cycle but these data are awaiting analysis and will be discussed elsewhere. The observations of 11-15 May were occasionally interrupted by small clouds or calibrations. Only three hours of data from 16 May are used, since clouds significantly interfere with the rest of the data from that day. A list of observations is given in Table 3.2, and in Figure 3.02 we plot a schematic diagram showing the temporal coverage of the observations. Note that the scan times shown in Table 3.2 (calculated from times stored directly into the raw data frames) spuriously decrease during the last day of the observing run; this problem originates with the tape drive storing the data and is removed during the data reduction.

No independent calibration data for the MCCD spectral camera are available for these observations. Although the MCCD instrument has a calibration flat field lamp, with the echelle grating and an order sorting prefilter in the beam the flat field lamp is not powerful enough to yield a good signal. The typical method for producing a spectral flat in cases like this is to rapidly scan the spectrograph grating while

exposing a frame in a region of quiet Sun, but since these observations required high precision velocities the spectrograph grating was not adjusted during the six days in order to improve its stability. The daily calibration data taken during the observing run consisted of ten randomly positioned scans of the quiet solar photosphere. These scans provide a spatial flat field when averaged to remove solar granulation; however the scans measure the photospheric spectrum and thus cannot provide a spectral flat field.

It is useful to examine the frequency characteristics of the observations. The data have a temporal frequency resolution $\Delta\nu \approx 5.4$ μHz, and a temporal Nyquist limit of $\nu_{Ny} \approx 5.4$ mHz. The data have a spatial Nyquist limit of $k_{Ny} \approx 6.2$ rad Mm^{-1}. The sunspot umbrae had radii of 12 and 6 Mm; from these values we can compute the spatial wavenumber resolution of the observations, Δk, as given by (Hill et al 1991)

$$\Delta k = \frac{2\pi}{N\ \Delta x} \tag{1}$$

where N is the number of resolution elements across the sunspot umbra, and Δx is the spatial step size of the observations. For the larger and smaller spot we have a spatial resolution of $\Delta k \approx 0.3$ rad Mm^{-1} and $\Delta k \approx 0.5$ rad Mm^{-1} respectively. It is helpful to understand these limits by placing them in the context of the global p-mode spectrum. What sort of features could we detect in the global p-mode spectrum with these limits? The resolution in spherical harmonic degree $L \equiv (l(l+1))^{1/2}$ is simply given by:

$$\Delta L = R_{\odot}\Delta k \approx 210 \tag{2}$$

Obviously we will not be able to resolve individual Y_m^l oscillation modes; this is simply because we are observing a very small region of the solar disk. Should we expect

to resolve any features in a diagnostic (k,ν) diagram? Following Braun et al (1992) we make a simple analysis to determine the visibility of the global p-mode ridges given the resolution limits of the data. We fit a ridge in the quiet-sun p-mode oscillation spectrum (as observed by Libbrecht and Kaufman, 1988) with a function $\nu(k,n)$, where k is the spatial wavenumber, and n is the radial quantum number of the particular ridge. We compute the number of resolution elements ($R_{ij}(k)$) separating the p-mode ridges with n=0 and n=1 for a given spatial resolution Δk as follows:

$$R_{01}(k) \equiv \frac{\nu(k-\Delta k,1) - \nu(k,0)}{\Delta\nu} \tag{3}$$

For $\Delta\nu$=5.4μHz and for $\Delta k \approx 0.3$ rad Mm^{-1} (the resolution for the observations of NOAA 6619) the value of R_{01} ranges from about 10 at $k \approx 1.0$ rad Mm^{-1} to about 80 at $k \approx 2.0$ rad Mm^{-1}; this is because the spacing between the ridges increases at higher wavenumber. With these spatial and temporal limits we could clearly separate the n=0 and the n=1 ridges; we say these two ridges are resolved. The next pair of ridges (n=1 and n=2) would be unresolved at $k \approx 1.0$ rad Mm^{-1} but easily resolved at $k \approx 2.0$ rad Mm^{-1}. If we use the spatial limit of the NOAA 6625 observations ($\Delta k \approx 0.5$ rad Mm^{-1}) we find that the n=0 and n=1 ridges are again resolved but the n=1 and n=2 ridges are unresolved. From this exercise we conclude that with perfect data we would resolve a few p-mode ridges with the NOAA 6619 data but we would resolve only one ridge in the NOAA 6625 data. Obviously because there will be noise in our measurements, we may not resolve ridges even if they exist.

A diagnostic (k,ν) diagram will be of some use; if sunspot umbra have a very distinct oscillation spectrum (perhaps with resonances at specific temporal or spatial

frequencies) we should see these phenomena in this data. However, if there are only subtle differences produced by the sunspot, such as shifts of the global p-mode ridges to different regions in the (k,ν) plane, we would be unlikely to detect such deviations with the temporal and spatial resolutions of this data. While the diagnostic (k,ν) diagram will be part of our analysis it has limited use and we must also employ other methods of analysis.

3. Data Reduction

In this section we discuss the data reduction used for these observations. Several different computer languages were used, including Fortran, *C* , and IDL (Interactive Data Language from Research Systems, Inc.) The reduction was developed and implemented on the IfA solar division Sun Microsystems computer network.

The data from the MCCD is written in a four-dimensional FITS file (Wells et al. 1981) as a time series of data cubes. The raw frames $I(x_{obs},\lambda)$ measure the intensity as a function of one observed spatial dimension (x_{obs}) and wavelength (λ). A set of these frames is collected by scanning the solar image in the orthogonal spatial dimension (y'_{obs}) to build a data cube $I(x_{obs},y'_{obs},\lambda)$. A new data cube is collected every 92 seconds and thus we develop a four dimensional data set $I(x_{obs},y'_{obs},\lambda,t)$. It is important to note that because of the scanning method the spatial dimension (y'_{obs}) is actually a function of time; thus we will use the prime notation.

The purpose of the data reduction is to produce a map of the solar velocity $v(x_{\odot},y_{\odot},t)$ from the observed data cubes $I(x_{obs},y'_{obs},\lambda,t)$, where x_{obs} and y'_{obs} are the

observed positions on the solar surface, and $x_\odot$ and $y_\odot$ are real positions on the Sun. The steps involved are (1) computing the Doppler shifts of several absorption lines $v_\lambda(x_{obs}, y'_{obs}, t)$, (2) removing image motion and solar rotation by interpolating to an even spatial grid $v_\lambda(x_\odot, y'_\odot, t)$, (3) averaging the velocities from several absorption lines $v(x_\odot, y'_\odot, t)$, and finally (4) interpolating the measured velocities onto an even time grid $v(x_\odot, y_\odot, t)$. Additionally we temporally filter the velocity data to isolate the five-minute period velocity oscillations.

In the following sections we discuss details of the data reduction. For the sake of clearity we divide our discussion into three sections and discuss the spatial, spectral and temporal operations although this order does not reflect the sequence of the data processing.

3.1. Image plane

There are two operations which are implemented in the image plane; removal of streaks caused by dust on the spectrograph slit (flat fielding) and interpolation onto an even spatial grid. Sharp intensity variations uniform in the scan dimension (y'_{obs}) appear as streaks in the image plane. These streaks are transmission variations along the spectrograph slit and are probably caused by dust. To precisely remove these streaks independent calibration data is needed but the image motion after the spectrograph slit would dictate that such calibrations be repeated often. It is possible to remove them without calibration data because these streaks are sharp and independent of the scan dimension (y'_{obs}) of the data cube. Computing the slit transmission vec-

tor is tricky since assumptions must be made in order to decouple the transmission induced intensity gradients from the real solar intensity gradients. The method we employ is the following: (1) a section of the image plane without large spatial gradients along the slit is selected, and averaged over (y'_{obs}) the scan dimension, (2) this mean intensity vector is fit with a sixth order polynomial, and then (3) the transmission vector is defined as the mean intensity vector divided by the polynomial fit. This method is used on every data cube and consistently gives good results.

To convert the observed coordinates into real solar coordinates we must correct for the residual instrumental motion and for the real solar motion in each data cube. To measure the residual image motion we compute the image centers for each data cube by fitting the spatial row (x_{obs}) and column (y'_{obs}) averages with second order polynomials. This residual motion is almost linear at a rate of 0.28 arcseconds hour^{-1} with an RMS deviation of 0.09 arcseconds. The real solar motion was measured during the observations using two other telescope systems at MSO, the Ca-K line telescope (Ronan and LaBonte, 1992) and the Stokes polarimeter (Mickey 1985). Correcting the drift and rotation measurements we interpolate the data onto an even spatial grid ($x_{\odot}, y_{\odot}$) with a grid spacing of 500 km (0.7 arcseconds). This interpolation is done with a simple bi-linear interpolation because it simplifies the temporal analysis of the data; however this method does not conserve flux and from simulations we estimate that only 3% of the RMS velocity flux is lost.

3.2. Spectral plane

The pertinent data reduction steps involving the spectral dimension of the data which we discuss include the lack of a spectral flat field and the implications on the analysis, the computation of Doppler shifts for each absorption line, and the averaging of the computed Doppler shifts to measure the umbral velocity.

Although there is no spectral calibration used the raw data appears flat because the MCCD Photometrics CCD camera has a very uniform response. Spectral features with contrast as small as 5% are clearly visible in the raw spectral frames, while no obvious camera defects are visible at this level. We examined the local spatial gradient of the sum of all 25,344 raw frames collected on 13 May 1991 and we found that the detector had randomly distributed pixel-to-pixel gain variations at only the 1% level or less. Since no reasonable spectral flat fielding technique was found we rely on the inherent uniform response of the CCD detector.

What is the effect of an uncorrected 1% gain variation in the intensity $I(x_{obs}, y'_{obs}, \lambda, t)$ on our computed velocities? Occurring in the continuum such a deviant pixel would have no effect since we extract each line profile individually; however with a wavelength drift in the data several umbral absorption lines will drift across this deviant pixel. The gain fluctuation will corrupt the apparent center of mass of the absorption line and thus remove our ability to compute an accurate central wavelength. This error has a spatial signature; such an error would be present in all scan positions (y'_{obs}) since one pixel on the detector measures $I(x_{obs}, \lambda)$ at all y'_{obs} positions at every time step. The error might not be equally present at all scan

positions since the continuum intensities and absorption line strengths change across the sunspot. The main contribution of this error would occur at low temporal frequencies, equivalent to the frequency of the wavelength drift; these frequencies are removed with the temporal filtering. However, the error would also influence the measurement of the five-minute period oscillations. As the deviant pixel moved from one line wing to the other the computed velocity amplitude of the oscillations would be reduced first in one direction and then in the other direction. The total effect would be to reduce the RMS amplitude of the velocity oscillation. We conclude that the main effect of not correcting for the random 1% gain variations of the spectral CCD camera is not to bias the computed velocity but to reduce the RMS amplitude of the velocity oscillations by some small factor.

In order to measure the Doppler shifts of the umbral spectra we use a cross-correlation technique. The most simple method to compute this shift would be to cross-correlate the whole slice of spectrum using all of the absorption lines at once. However this method is subject to biases from small continuum features and noise in the spectrum because the absorption lines are so weak. (The measured equivalent widths of the umbral lines range from 1.3 to 22.1 mÅ, whereas the expected photon noise in the umbral spectra would correspond to an equivalent width of 0.5 mÅ.) To avoid noise from continuum features we extract individual absorption line profiles from each spectrum and cross-correlate these profiles against a reference profile of that absorption line. This results in a Doppler measurement for each absorption line at each spatial pixel, $v_\lambda(x_{obs}, y'_{obs}, t)$.

We define a reference umbral absorption profile $I_n(\lambda)$ for each absorption line as the average of the spectra from all spatial pixels located interior to an intensity contour in the first data cube of each day of data. Using this reference profile and the extracted profile from each spectrum $I_n(x_{obs}, y'_{obs}, \lambda, t)$ we compute the discrete cross-correlation function $C_n(j,t)$ as follows:

$$C_n(j,t) = (N(j))^{-1} \sum_{\lambda_i=\lambda_{0,n}-\lambda_{max}}^{\lambda_{0,n}+\lambda_{max}} I_n(\lambda_i)\, I(x_{obs}, y, \lambda_i - j, t) \tag{4}$$

where $\lambda_{0,n}$ is the central wavelength index of the nth absorption profile and the normalization $N(j)$ is the number of overlapping points for each lag j. For this reduction λ_{max} was set to 0.126Å (6.1 km s^{-1}) and the maximum lag values used in the cross-correlation computing were 0.098Å (4.7 km s^{-1}). The discrete cross-correlation points were fit with a parabola and the center of this parabola was defined as the Doppler shift of the absorption line.

The Doppler shift from each umbral absorption line is averaged to form one umbral velocity time series; similarly the Doppler shifts for both photospheric Fe I lines are averaged to form an Fe I velocity time series. All the absorption lines are used in the process; but a threshold velocity of 135 m s^{-1} is used to remove spikes from the velocity time series. (This threshold was determined by examining a histogram of all the umbral velocity measurement and removing the extreme points in the distribution; this value removes the upper and lower 1% of the measurements.) The main source of noise which produces spikes in the umbral velocity time series is the mismanagement of measurement drop-outs by the temporal filtering routine; such drop

outs are caused when stray light completely fills the umbral absorption line and prevents a valid Doppler shift measurement. No thresholds are used during the averaging of the Fe I lines because the photospheric absorption line profiles do not suffer such contamination.

3.3. Time domain

There are two important reduction steps which are implemented in the time dimension. The first is a temporal filter which removes the low frequency noise power. As in Libbrecht and Zirin (1986), a gaussian running mean is computed from the data with the equation:

$$\bar{v}\,(x_{\odot},y_{\odot},t_i) = (N)^{-1} \sum_{\Delta t=-T}^{T} v(x_{\odot},y_{\odot},t_i+\Delta t) \left[e^{-\Delta t^2/2\tau^2} - e^{-T^2/2\tau^2} \frac{(1-(\Delta t^2 - T^2))}{(2\tau^2)} \right] \qquad (5)$$

where τ=3 (4.6 minutes), T=5 (7.6 minutes), and N is a normalization factor defined by:

$$\mathrm{N} = \sum_{\Delta t=-T}^{T} \left[e^{-\Delta t^2/2\tau^2} - e^{-T^2/2\tau^2} \frac{(1-(\Delta t^2 - T^2))}{(2\tau^2)} \right] \qquad (6)$$

At the beginning and end of the observing interval, the limits $\pm T$ is changed such that the residual velocity $v - \bar{v}$ goes smoothly to zero, apodizing the data in the time domain. The frequency response of this temporal filtering is shown in Fig 3.03; basically the filter is a high pass filter which is transparent above a frequency $v \approx 2$ mHz.

The second important operation in the time domain is shifting the velocity data onto an even time grid. Each spatial pixel has a unique time associated with it, easily calculated since the spatial interpolation is a simple bi-linear operation. This time is

used in a cubic spline algorithm to interpolate the velocity time series from each pixel onto an even time grid with an interval of exactly 92.0 seconds. Tests done before and after this cubic spline interpolation show that the oscillation power spectrum has identical oscillation peaks with the same power at the same frequencies; we are confident the algorithm properly shifts the velocity scans to an even time grid producing temporal snapshots of the velocity field.

3.4. Characteristics of the umbral spectra

Sample photospheric and umbral spectra are shown in Figure 3.04. Some of the umbral absorption lines used in this study can be identified with transitions of the molecules of TiO, CaH and CN (Boyer et al 1975); we list these identifications along with other information in Table 3.3. The two photospheric lines used in the study correspond to two Fe I absorption lines, at λ6400.0Å and λ6400.3Å. These lines have magnetic splitting coefficients $g_{eff} = 1.25$ and $g_{eff} = 1.43$ respectively. In Fig 3.05 we plot the equivalent width of a strong umbral line (a TiO/CN blend at λ6405.45 Å) versus the continuum intensity for each spatial pixel in a scan of the umbra of NOAA 6619 and the nearby photosphere. There is a strong correlation between the line strength and the continuum intensity and the line is not measurable where the continuum intensity is greater than 0.48 times the photospheric intensity. The umbral lines are confined to the umbra and the inner penumbra and thus the velocity we measure with these lines solely reflects the motion of plasma in these regions of the solar surface.

Clearly the umbral absorption lines are concentrated in the sunspot umbrae on the solar surface; are they similarly concentrated in a narrow height range of the umbral atmosphere? Theoretical work by Avrett and Kurucz (1983) suggest that the molecular lines in a sunspot are formed in the temperature minimum of the umbral atmosphere (this height is exactly equivalent to the quiet-sun photosphere after accounting for the Wilson depression of sunspot umbrae). This means that all the molecular absorption lines are formed at the same height and thus measure the same velocity field. We can test the velocity data directly for phase shifts to see if this is true; however because of noise in the time series of individual line shifts we produce two umbral line velocity signals by averaging the velocity from two random sets of five umbral lines. In Fig 3.06 these two velocities are plotted from 13 May 1991 data and we see that the velocities are strongly correlated along the line with slope of one, with a scatter of $\pm$ 20 m s^{-1}. This scatter corresponds to an error of about $\pm$ 0.1 pixels in the original calculated shift of individual absorption lines. This is a reasonable expectation for the shift measurement error; we suggest that the measurement error alone accounts for the scatter seen in the two umbral line velocities and that there is no additional scatter introduced by a phase shift. Thus for the purposes of this work we assume that all of the umbral absorption lines are formed at the same height in the sunspot umbrae and measure identical velocity fields.

The same conclusion cannot be drawn from a comparison of the umbral absorption line velocity with the Fe I absorption line velocity. Fig 3.07 shows the velocity computed from the two Fe I absorption lines versus the velocity from the average of

all the umbral absorption lines. This diagram shows only a weak correlation between the two velocity signals, and we conclude that the Fe I absorption lines measure a different velocity field than that measured by the umbral lines.

4. Spatial Analysis of Umbral Oscillations

In this section we discuss the procedures used to analyze the spatial and temporal characteristics of the umbral velocity oscillations. The first and most basic analysis is to simply average the velocity from each pixel inside the umbra (as defined by an intensity threshold) to produce the mean umbral velocity $v_{umbra}(t)$:

$$v_{umbra}(t) = \frac{1}{N_{umbra}} \sum_{umbra} v(x_{\odot}, y_{\odot}, t) \tag{7}$$

We will make use of this velocity in some of the more involved analyses. The analyses we discuss below are (1) the mapping of the root mean square (RMS) velocity inside the umbrae, (2) the search for natural umbral oscillation modes with a Fourier-Bessel analysis, (3) the calculation of a diagnostic (k,ν) diagram and (4) an analysis of azimuthally symmetric ingoing and outgoing wave power inside the umbrae.

4.1. RMS Velocity Maps

We take all the velocity maps for each sunspot and compute the RMS velocity distribution given by:

$$V^{(1)}_{RMS}(x_{\odot}, y_{\odot}) = \left[\frac{1}{(N_t - 1)} \sum_{t=0}^{N_t - 1} v^2(x_{\odot}, y_{\odot}, t) \right]^{1/2} \tag{8}$$

Since the data is temporally filtered only velocity oscillations with frequencies between 2 and 5.4 mHz will contribute to $V^{(1)}_{RMS}$; however all spatial wavenumbers

contribute to the velocity.

The next step in the direct mapping is to remove the mean umbral velocity $v_{umbra}(t)$ from the data to produce a new RMS velocity

$$V^{(2)}_{RMS}(x_{\odot},y_{\odot}) = \left[\frac{1}{(N_t-1)}\sum_{t=0}^{N_t-1}(v(x_{\odot},y_{\odot},t)-v_{umbra}(t))^2\right]^{1/2} \tag{9}$$

The data is now spatially filtered so that waves which are flat on the size scale of the umbral diameter, with $\lambda >> 2r_{umbra} \approx 24$ Mm or $k << 2\pi/\lambda \approx 0.26$ rad Mm $^{-1}$ are removed.

4.2. Fourier-Bessel Analysis

We will assume that a sunspot is cylindrically symmetric (NOAA 6625 is a close approximation) and no damping of the acoustic waves occurs inside the sunspot. Solutions to the wave equation in cylindrically symmetric coordinates yield Bessel functions $J_m(kr)$. We construct a set of Bessel functions and perform a Fourier-Bessel decomposition of the velocity field inside the umbra of sunspot NOAA 6625. We analyze the temporal power spectrum of each Bessel mode searching for resonant frequencies.

We construct a set of complex Bessel function masks in two dimensions ($\tilde{M}_{m,n}(r,\theta)$) according to:

$$\tilde{M}_{m,n}(r,\theta) \equiv J_m((\kappa_{m,n}/a)r)\, e^{im\theta} \tag{10}$$

where $\kappa_{m,n}$ is the nth zero of the Bessel function J_m and $a = r_{umbra} \approx 7$ Mm, the umbral radius (we use Bessel functions with azimuthal order $0 \le m \le 7$ and with radial order $1 \le n \le 8$. We normalize these masks with a constant $\tilde{N}(m,n)$ determined

with the Bessel normalization condition (Arfken, 1970)

$$\tilde{N}(m,n) \equiv \int_0^{2\pi} \int_0^a [\tilde{M}_{m,n}]^2 \, r \, dr \, d\theta = \frac{a^2}{2} [J_{m+1}(\kappa_{m,n})]^2 \tag{11}$$

The real part of the normalized Bessel masks is displayed in Fig 3.08; We test the orthogonality of the Bessel masks by computing the overlap matrix $\tilde{C}_m(n,nn)$ for each azimuthal order m as :

$$\tilde{C}_m(n,nn) \equiv \int_0^{2\pi} \int_0^a \tilde{M}_{m,n}(r,\theta) \, \tilde{M}_{m,nn}(r,\theta) \, r \, dr \, d\theta \tag{12}$$

where n and nn signify different radial orders. For the masks used in the Fourier-Bessel analysis of NOAA 6625, there is significant overlap as can be seen in the overlap matrix for the real part of azimuthal order $m = 2$:

$$| \, REAL(\tilde{C}_2(n,nn)) \, | = \begin{bmatrix} 100 & 19 & 1 & 1 & 0 & 0 & 0 & 0 \\ 19 & 57 & 15 & 1 & 1 & 0 & 0 & 0 \\ 1 & 15 & 40 & 12 & 0 & 1 & 0 & 0 \\ 1 & 1 & 12 & 31 & 10 & 0 & 1 & 0 \\ 0 & 1 & 0 & 10 & 25 & 9 & 0 & 1 \\ 0 & 0 & 1 & 0 & 9 & 21 & 8 & 0 \\ 0 & 0 & 0 & 1 & 0 & 8 & 19 & 7 \\ 0 & 0 & 0 & 0 & 1 & 0 & 7 & 16 \end{bmatrix} x\,10^{-2} \tag{13}$$

This overlap is due to undersampling of the masks.

We compute the Fourier-Bessel components $\tilde{b}_{m,n}(t)$ as a complex variable:

$$\tilde{b}_{m,n}(t) \equiv \frac{2}{N(m,n)} \int_0^{2\pi} \int_0^a \mathrm{v}(r,\theta,t) \, \tilde{M}_{m,n}(r,\theta) \, r \, dr \, d\theta \tag{14}$$

where $\mathrm{v}(r,\theta,t)$ (computed from $\mathrm{v}(x_{\odot},y_{\odot},t)$) is the measured umbral velocity. We then compute the discrete Fourier transform of these fit coefficients;

$$\tilde{b}_{m,n}(\mathrm{v}) = \frac{1}{N_t} \sum_{t=0}^{N_t-1} \tilde{b}_{m,n}(t) \, e^{(-2\pi i \mathrm{v} t / N_t)} \tag{15}$$

We finally compute the power spectra for each Bessel component $P_{m,n}(\mathrm{v})$. Because of the non-orthogonality of the masks used in this analysis there is a leakage of power

from one Bessel component into another. However, due to the sharp drop of the measured oscillation power with order m and radial order n (or equivalently a sharp drop in the measured power with wavenumber) it is possible to remove most of this inter-mode leakage.

4.3. Calculation of a Diagnostic Diagram

The calculation of a diagnostic (k,ν) diagram amounts to a three dimensional Fourier transform of the oscillation data. First each velocity image is multiplied by a circular aperture, which is apodized at the edge to go smoothly to zero. This mask is centered on the sunspot with a radius defined to match the umbral radius. The mean umbral velocity $v_{umbra}(t)$ is subtracted from each snapshot to prevent spatial frequency aliasing and this masked velocity snapshot is Fourier transformed. First, the 2-d discrete Fourier transform of the data is computed for the spatial coordinates:

$$\tilde{V}(k_x,k_y,t) = \frac{1}{N_x N_y} \sum_{x=0}^{N_x-1} \sum_{y=0}^{N_y-1} v(x_{\odot},y_{\odot},t) e^{-2\pi i\left[\frac{k_x x}{N_x}+\frac{k_y y}{N_y}\right]} \tag{16}$$

Then at each spatial frequency (k_x,k_y) a discrete 1-d transform is computed as above to give $\tilde{V}(k_x,k_y,\nu)$ (these steps are used for reasons of computational efficiency). Next the power at each point $P(k_x,k_y,\nu)$ is computed. Finally, power at spatial frequency (k_x,k_y) is interpolated onto circles given by

$$k_r^2 = k_x^2 + k_y^2 \tag{17}$$

This results in a diagnostic diagram for the umbral oscillation power $P(k_r,\nu)$.

4.4. Radial Analysis - Ingoing vs Outgoing

We perform a traveling wave analysis of umbral velocity in each sunspot. First we average the velocity azimuthally for each velocity time step, producing a single vector $\bar{v}(r,t)$. We then perform a discrete Fourier transform on this data as follows:

$$\tilde{V}(k_r,\nu) = \frac{1}{N_r N_t} \sum_{r=0}^{N_r-1} \sum_{t=0}^{N_t-1} \bar{v}(r,t) e^{-2\pi i \left[\frac{k_r r}{N_r} + \frac{\nu t}{N_t}\right]} \tag{18}$$

and then we compute the power spectrum $P(k_r,\nu)$. We then average over the appropriate temporal and spatial frequencies to produce the total ingoing power (P_{in}) and total outgoing power (P_{out}).

Next we examine the spatial behavior of the ingoing and outgoing power. We define a set of circular disks centered on the umbrae having increasing radii r (see Fig 3.09). We perform the traveling wave analysis in each disk and define an absorption factor $\alpha(r)$ for each circular disk with radius r as follows:

$$\alpha(r) \equiv \frac{P_{in}(r) - P_{out}(r)}{P_{in}(r_{umbra})} \tag{19}$$

where r_{umbra} is the size of the sunspot umbra. This absorption factor represents the integrated absorption of acoustic power from the umbral center to radius r; the spatial variation of the absorption within the sunspot umbra is related to the radial derivative of this factor, $\partial\alpha(r)/\partial r$.

5. Discussion - the Nature of the Umbral Oscillations

In Figure 3.10 we plot the mean umbral velocity, $v_{umbra}(t)$, for the observations of NOAA 6625. This figure shows a very strong oscillation with roughly a five

minute period, and a slower beat pattern in the velocity which suggests that we are seeing oscillations closely spaced in frequency. A power spectrum of this data is shown in Fig 3.11 and indeed there are several closely spaced peaks of oscillation power in the five-minute band from 2.0 to 4.0 mHz. Simply summing the power over the five-minute period frequency band (in this case 2.0 to 4.0 mHz) in a method identical to Lites 1992 gives an RMS velocity of 71.5 m s^{-1}, consistent with the mean of the seven observations Lites quotes. The highest power peaks in our data are roughly between 3.0 and 5.1 x 10^4 m^2 s^{-2} Hz^{-1}, and the average high frequency noise is about 0.2 x 10^4 m^2 s^{-2} Hz^{-1}.

It is important to note that none of these power peaks are well resolved in the data even with the temporal resolution of 5.4 μHz provided by the observations. Analysis of small segments of the full velocity time series show that the power distribution among the set of peaks appears to change. We do not ascribe this behavior to a real variation in the frequencies of the driving source of these oscillations nor to a temporal switching among oscillation modes (Lites 1986); instead we state that this behavior is a natural consequence of the fact that the oscillation power peaks are not resolved by the observations (also Lites 1986). The most rigorous analysis we can perform on this power spectrum is to measure the behavior of the envelope of the power of the oscillations; the envelope is consistent with the measured distribution of power of the global p-modes (Korzennik, 1990) when the global p-modes are summed over a similar range in wavenumber.

Is the driving source of these oscillations located inside or outside the sunspot?

The conclusion we must draw from these observations is that the source of the oscillations is located outside the sunspot; in fact we conclude that the oscillations themselves are a direct manifestation of the global p-modes traveling through the sunspot umbrae. There are three observations which support this conclusion: (1) the similarity of the spatial and temporal characteristics of the oscillations inside the sunspot with the global p-mode oscillations, (2) the apparent decay of the amplitude of the high wavenumber oscillations inside the umbra of the sunspot, and (3) the excess power of ingoing waves compared to outgoing waves in the sunspot umbrae.

The diagnostic (k,ν) diagrams for the spot umbrae show that the internal umbral oscillations have spatial and temporal characteristics which are identical to the global p-modes, within the resolution provided by the data (see Figure 3.13). The internal umbral oscillation power is bounded by the n=0 ridge given by the relation $\nu = (k/0.14)^{1/2}$ with ν in units of mHz and k in units of rad Mm^{-1}; this ridge is also known as the f-mode and represents buoyancy waves on the surface of the Sun with a dispersion $\omega^2 = g_{\odot}k$ (Hill et al. 1991). For a given frequency no significant power is seen at wavenumbers larger than the wavenumber of the n=0 ridge. This result is inconsistent with the conclusion of Abdelatif et al. (1987). These authors state that there is no power transmitted into the umbra with a horizontal phase speed less than 25 km s^{-1}. At ν=3.2 mHz this phase speed cutoff means there should be no power beyond the spatial wavenumber k=0.8rad Mm^{-1}; but from Figure 3.13 we can see power out to a spatial frequency of k=1.8rad Mm^{-1}, three resolution elements beyond

the predicted cutoff. We stress that in deriving this cutoff speed, Abdelatif et al. used properties of the oscillations at frequencies above and below the five-minute frequency band where noise greatly affects the data whereas our measurements are limited to the five-minute band where our signal seems most meaningful.

Although no ridges are seen in the umbral (k,ν) diagrams, the power is distributed in a manner consistent with unresolved ridges. Most importantly, there are no strong absorptions or emissions at isolated spatial wavenumbers or temporal frequencies. The power in the lowest wavenumber bin $0 \leq k < 0.2$ rad Mm^{-1} rises from 2 mHz (the temporal filter cutoff) to a peak at 3.2 mHz as ν^3 and then falls as ν^{-5} reaching insignificant levels at 4.1 mHz. These power laws are consistent with the power distribution of the global p-mode oscillation spectrum (Korzennik, 1990)

The second observation supporting the idea of an external source is the radial behavior of the RMS velocity of the umbral oscillations as shown in Figure 3.12. The total RMS velocity $V^{(1)}_{RMS}$ is constant across the umbra and the inner penumbra, with an amplitude of roughly 15 m s^{-1}. (This result is consistent with the work of Balthasar et al. (1988). These authors show power spectra of the oscillations in a slice across a sunspot umbra and penumbra; the power in the five-minute band is roughly constant across the umbra and inner penumbra.) More importantly, the high wavenumber RMS velocity $V^{(2)}_{RMS}$ displays a drop from the edge of the penumbra to the center of the umbra, decreasing by roughly 5 m s^{-1} in the umbral center. (This is consistent with the measured RMS amplitude of v_{umbra}, see Figure 3.10.) If the oscillations seen in the umbra are quiet-sun p-modes traveling through the sunspot, then

removing the mean umbral velocity from the time series leaved waves that have one or more nodes (or peaks) within the umbra. These high wavenumber waves show a radial RMS profile ($V^{(2)}_{RMS}$) which suggests that the amplitudes are damped as they travel through the sunspot umbrae. It is known that waves with $k < 0.3$ rad Mm $^{-1}$ are not efficiently absorbed by sunspots (Braun et al. 1987), so it is not surprising that the total RMS velocity distribution $V^{(1)}_{RMS}$ in the umbra is constant.

The final and the strongest evidence supporting our conclusion comes from the traveling wave analysis. The traveling wave analysis shows an excess in power traveling inward toward the center of the umbra. The total absorption factor $\alpha(r_{umbra})$ is 0.21 ±0.02 for NOAA 6619 and 0.19 ±0.02 for NOAA 6625. The spatial dependence of the absorption factor (see Fig 3.14) shows an increase with distance from the umbral centers. Following Braun (1988) we can define an acoustic opacity $\chi(r)$ with the equation

$$\frac{dP(r)}{P(r)} = -\chi(r)dr \tag{20}$$

The simplest solution for the acoustic opacity, a constant term $\chi(r) = \chi_0$ leads us to the solution (See Appendix B)

$$\alpha(r) = \chi_0 r \tag{21}$$

From Figure 3.14 we can see that by approximating the absorption function with a straight line, we compute a value of $\chi_0 \approx 0.03\text{Mm}^{-1}$ for both NOAA 6625 and NOAA 6619. While the absorption functions in Figure 3.14 are more complicated than linear functions, it is unclear whether this is due to the non-circular shape of the umbrae or a real absorption effect.

This conclusion is the first observational proof of the accepted theory about the source of the umbral oscillations (Thomas 1981), and it negates other theories suggesting that the umbral oscillations were driven by phenomena within the sunspot itself, such as oscillatory convective motions (Moore 1973). We have not used this data to directly study umbral granulation; because umbral granulation has a lifetime of 1500 sec (0.7 mHz) (Beckers and Schroter 1968) it is removed by our temporal filtering.

Is there an umbral acoustic cavity which produces resonances in the photospheric umbral oscillations?

The conclusion we reach is no, we do not observe resonant oscillation modes which might reflect the existence of a sub-photospheric resonant cavity, (at least to the level of 10^{4} m^2 s^{-2} Hz^{-1}). The observational proof of this conclusion is two-fold: (1) we see no resolved modes nor any system of power peaks in the Fourier-Bessel analysis of the NOAA 6625 oscillations and (2) we see no resonant behavior in the diagnostic (k,ν) diagram of the oscillations in either sunspot umbrae. This conclusion suggests that interpretation of umbral oscillation power peaks as modes of the umbral cavity (Campos 1989) may be incorrect.

The Fourier-Bessel analysis shows no strong evidence for natural oscillation modes of the umbra of NOAA 6625; the power spectrum for the lowest mode (and successively higher modes) is not significantly different from the power spectrum for the mean umbral velocity. (see Figure 3.11) If there were standing modes inside the

sunspot umbra, we would expect to see a set of peaks representing the eigenfrequencies of the umbral cavity. For example, electromagnetic waves in a cylindrical resonant cavity with a depth dz and a radius a show resonant peaks with a frequency spacing equal to a constant times $\left[\frac{\kappa_{m,n}}{a} + \frac{\pi^2 p^2}{dz^2}\right]^{1/2}$ (Arfken, 1970) where $\kappa_{m,n}$ is the nth zero of the Bessel function J_m a is the umbral radius, and p is related to the number of nodes in the z direction. Although the real umbra is more complicated than a simple cylinder, one might still expect to see power peaks with some sort of regular spacing. The data do not show this behavior. Only a few Bessel modes have significant power above the high frequency noise level; most of the observed oscillatory power is contained in modes with $0 \leq m \leq 2$ and $1 \leq n \leq 3$ (see Figure 3.08). This only reflects the steep drop of observed power with increasing spatial wavenumber and is not a property of the modes themselves.

What is the connection between the umbral oscillations and the absorption of photospheric p-mode oscillations?

The answer we uncover is that the photospheric umbral oscillations are the global p-mode oscillation being absorbed inside the umbrae. The fact that the absorption is spatially resolved helps to distinguish among theories explaining p-mode absorption by sunspots. We can certainly rule out the most simple monolithic spot which undergoes a resonant acoustic absorption in a thin transition region (Hollweg 1988) since this absorption would not occur uniformly across the sunspot umbrae. Of course an ensemble of smaller flux tubes spread across the inside the umbra, each resonantly

absorbing incident acoustic power is consistent with our data. Similarly, many other theories concerning p-mode absorption by sunspots (for example see Lou 1990, Spruit and Bogdan 1992, LaBonte and Ryutova 1992) are consistent with our data, since they predict the absorption occurs over a large spatial region. Realistically better observations of this type will be needed before meaningful constraints can be added to these theories.

6. Summary and Implications for Future Work

We have made long time series observations of two sunspot umbrae using pure umbral absorption lines to study the photospheric umbral velocity oscillations. The following properties of the umbral oscillations are observed:

(1) There is more power traveling toward the centers of the umbrae than leaving the umbral centers; the absorption factor is roughly 0.2 for both umbrae.

(2) The oscillations have very detailed spectra which are not resolved with our data, though our frequency resolution is good ($\Delta\nu$=5.4μHz).

(3) The spatial and temporal properties of the oscillations inside the umbrae are indistinguishable from the known properties of the global p-mode oscillations outside the sunspots.

(4) The total RMS velocity is constant across the sunspot umbrae; however the RMS velocity of the higher spatial wavenumber waves decreases from the edge of the penumbra to the center of the umbra.

(5) There are no resolved power peaks nor any system of power peaks in a Fourier-Bessel decomposition of the oscillations in the round umbra of NOAA 6625.

We use these observations to make the following conclusions about the physical nature of the photospheric umbral oscillations:

(1) The umbral oscillations are driven by an external source: that source has spatial and temporal characteristics identical to the global p-mode oscillations.

(2) There is no photospheric acoustic cavity producing a resonant spectrum of natural umbral oscillations.

(3) The p-mode absorption process is directly measurable; a linear fit to this absorption shows that the power may be removed uniformly from the oscillatory waves as they travel across the sunspot umbrae.

We feel that the techniques used in this work have strong implications for future studies of the photospheric umbral oscillations; the important issue is the difference in the velocity field measured with the pure umbral lines and the photospheric Fe I lines. The photospheric line velocities are very susceptible to contamination from the stronger photospheric velocity field outside the sunspot (due to stray light), and we feel that this contamination accounts for the observed velocity differences. Future observations aimed at measuring the umbral velocity field must use the pure umbral absorption lines if this contamination is to be avoided.

Finally many quasi-stationary flow fields are present in and around sunspots (see Chapter 1). The apparent frequency of a propagating wave is shifted if it travels

through a moving medium, and in this way the quasi-stationary velocity fields of sunspots can be probed at depth by observing traveling waves in and around sunspots. An analysis similar to the one performed by Braun et al., limited to azimuthally symmetric waves ($m = 0$) has the potential to reveal the depth behavior of the photospheric moat flow by precisely comparing the frequencies of the ingoing and outgoing p-mode waves. Such an detailed analysis conducted inside a sunspot umbra could reveal similar information concerning the umbral inflow velocities discussed above; however there must be characteristic umbral oscillations to measure a frequency shift against, and such an umbral acoustic dispersion has not yet been seen. These proposed studies would require precise measurements of the oscillations with frequency measured errors less than 1%.

References

Abdelatif, T.E., Lites, B.W. and Thomas, J.H. : 1986, *Astrophys. J* **311** , 1015.

Arfken, G. : 1970, *Mathematical Methods for Physicists* , 2nd Edition, (Academic Press, New York, San Francisco and London)

Avrett, E.H. and Kurucz, R.L. : 1983, *Inst. Theor. Astrophys. Report No. 59,* ed. O. Hauge, Institute of Theoretical Astrophysics, Blindern, Oslo, p43.

Balthasar, H., Fangmeier, E., Kuveler, G. and Wiehr, E. : 1988 in *Advances in Helio- and Asteroseismology* eds J. Christensen-Dalsgaard and S. Frandsen, I.A.U. Symp. #123, 183.

Beckers, J.M. and Schroter E.H. : 1968, *Solar Physics* **4** , 303.

Beckers, J.M. and Schultz, R.B. : 1972, *Solar Physics* **27** , 61.

Bhatnagar, A., Livingston, W.C., and Harvey, J.W. : 1972, *Solar Physics* **27** , 80.

Boyer, R., Sotirovski, P., Harvey, J.W. : 1975, *Astron. Astrophys. Suppl* **19** , 359.

Braun, D.C., Duvall, T.L., and LaBonte, B.J. : 1987, *Astrophys. J* **319** , L27.

Braun, D.C. : 1988, *The Interaction of High-Degree p-Mode Oscillations with Solar Active Regions* Ph. D. dissertation, Univ. of Hawaii

Braun, D.C., Duvall, T.L., LaBonte, B.J., Jefferies, S.M., Harvey, J.W., Pomerantz, M.A. : 1992, *Astrophys. J* **391** , L113.

Campos, L.M.B.C. : 1989 *Mon. Not. Roy. Astro. Soc.* **241** , 215.

Hill, F., Deubner, F.L., and Isaak, G. : 1991, in *Solar Interior and Atmosphere* , eds A.N. Cox, W.C. Livingston and M.S. Matthews, (The University of Arizona Press, Tucson), p338.

Hollweg, J.V. : 1988, *Astrophys. J* **335** , 1005.

Howard, R. : 1967, *Solar Physics* **2** , 3.

Kobanov, N.I. : 1990, *Solar Physics* **125** , 25.

Korzennik, S.G. : 1990, *Seismic Analysis of the Sun from Intermediate and High Degree p-Modes* Ph. D. dissertation, UCLA

Leighton, R.B., Noyes, R.W., and Simon, G.W. : 1962, *Astrophys. J.* **135** , 474.

Libbrecht, K.G. and Zirin, H. : 1986, *Astrophys. J.* **308** , 413.

Libbrecht, K.G. and Kaufman, J.M. : 1988, *Astrophys. J.* **324** , 1172.

Lites, B.W. : 1986, *Astrophys. J.* **301** , 992.

Lites, B.W. : 1992, in *The Theory of Sunspots* , eds J.H. Thomas and N.O. Weiss, *in press.*

Livingston, W. and Mahaffey, C. : 1981, in *The Physics of Sunspots,* eds L.E. Cram and J.H. Thomas (Sunspot, NM: National Solar Observatory), 312.

Mickey, D.L. : 1985, *Solar Physics* **97** , 223.

Moore, R.L. : 1981, *Space Sci. Rev.* **28** , 387.

Penn, M.J., Mickey, D.L., Canfield, R.C., LaBonte, B.J. : 1991, *Solar Physics* **135** , 163.

Rice, J.B. and Gaizauskas, V. : 1973, *Solar Physics* **32** , 421.

Ronan, R.S. and LaBonte, B.J. : 1992, *Astrophys. J., submitted.*

Thomas, J.H. : 1981, in *The Physics of Sunspots,* eds L.E. Cram and J.H. Thomas (Sunspot, NM: National Solar Observatory), 345.

Thomas, J.H., Cram, L.E., and Nye, A.H. : 1982, *Nature* **297** , 485.

Thomas, J.H. : 1985, *Aust. J. Phys.* **38** , 811.

TABLE 3.1

Observing Parameters for May 1991 Umbral Observations

MCCD Parameter	Value
Spatial number (pixel)	64
Scan number (pixel)	64
Spatial range (arcsec)	38 x 38
Spatial scale (arcsec pixel^{-1})	0.6
Spectral position (Å)	6404
Spectral number (pixel)	576
Spectral range (Å)	8.1
Spectral dispersion (Å pixel^{-1})	0.014
Slit width (μm)	56
Grating	echelle
t_{expos} (ms)	480

TABLE 3.2

Observations for May 1991 Umbral Oscillations Study

Date (May 1991)	Sunspot (NOAA)	Position ($R_\odot$)	Duration	N_{image}	t_{scan} (sec)
11	6619	0.55	7h 20m	283	92.1
12	6619	0.58	6h 00m	224	92.1
13	6619	0.69	10h 08m	396	92.1
14	6625	0.29	10h 18m	400	92.1
15	6625	0.49	11h 37m	447	92.1
16	6625	0.63	6h 48m	280	87.3

TABLE 3.3

The Umbral Spectrum of NOAA 6619

λ_{obs}	Eq. Width	Best Match		Error
(Å)	(mÅ)	Molecules	λ_{Boyer} (Å)	$\lambda_{Boyer} - \lambda_{obs}$
6400.63	≈ 6	TiO, CaH	6400.61	-0.02
6400.98	12.4	CaH	6401.02	+0.04
6401.46	16.0	TiO, TiO	6401.50	+0.04
6401.95	13.9	?	-	-
6402.42	≈ 13	TiO, CN	6402.41	-0.01
6403.00	10.3	TiO, CaH, CN	6403.05	+0.05
6403.71	22.1	?	-	-
6404.13	2.9	?	-	-
6404.52	12.3	TiO, CN	6404.50	-0.02
6404.77	5.0	?	-	-
6405.11	6.3	?	-	-
6405.45	18.4	TiO, CN	6405.43	-0.02
6405.77	5.4	?	-	-
6406.64	7.9	CN	6406.66	+0.02
6406.87	8.4	TiO, TiO	6406.88	+0.01
6407.17	10.1	?	-	-
6407.41	1.3	?	-	-
6407.81	≈ 18	CaH, CN	6407.77	-0.04

Figure 3.01 The main umbrae of NOAA 6619 and NOAA 6625. In each wide field view we see the whole sunspot and a section of the surrounding photosphere. In each inset we show a continuum image of the region scanned by the MCCD spectrograph; for this data the field of view is limited to the center of the sunspots.

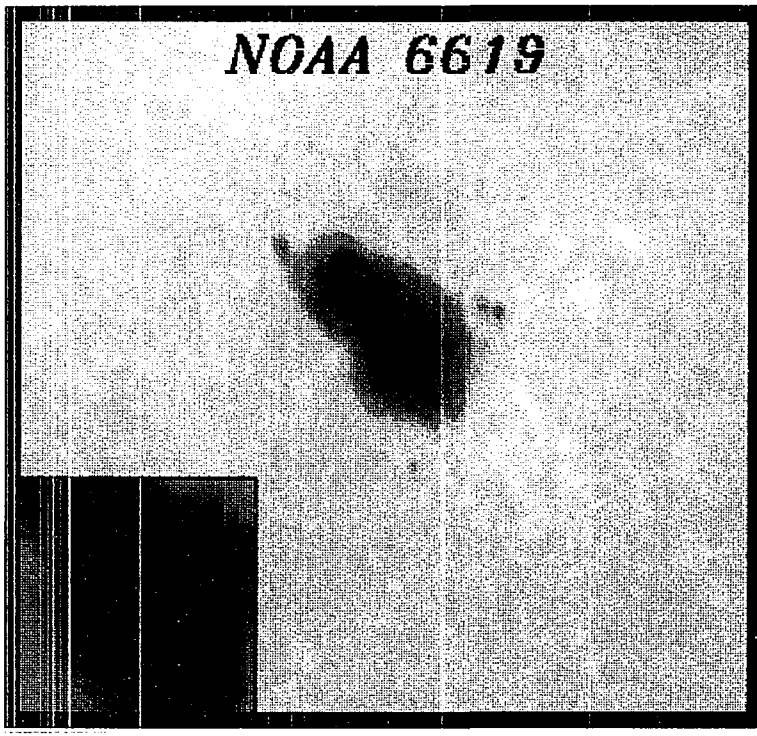
NOAA 6619

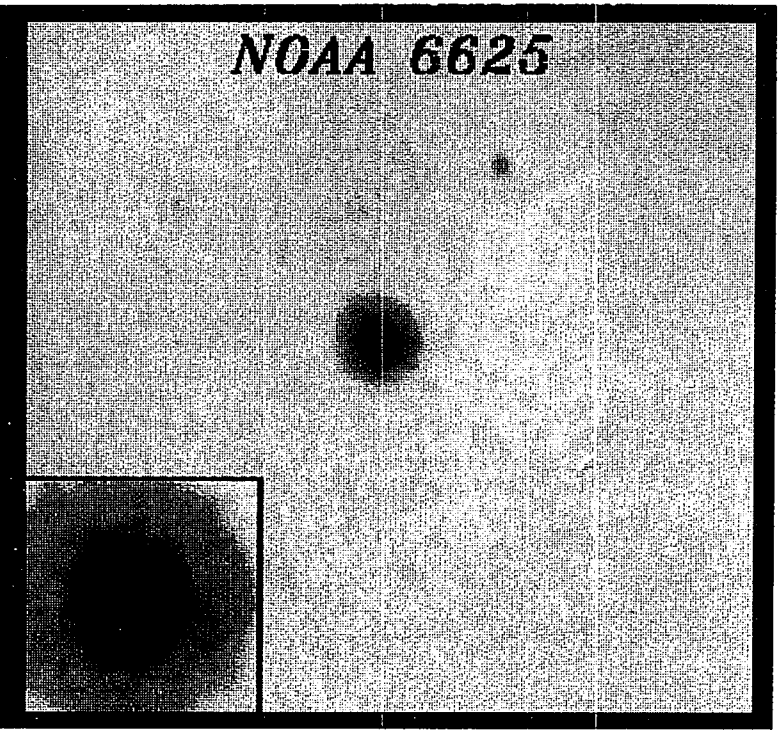
NOAA 6625

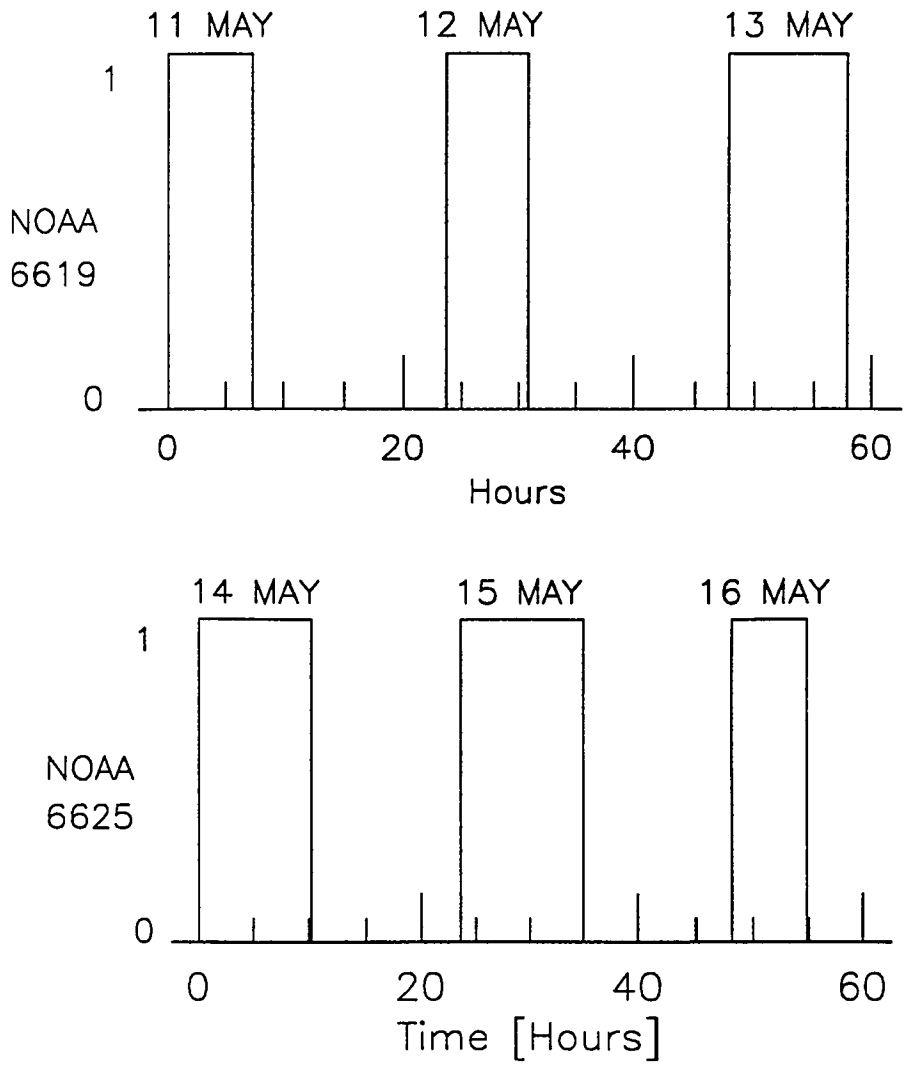

Figure 3.02 Time-line of the observations of the two sunspot umbrae. In the figure we plot a value of 1 at times with observations and a 0 during times without data (night and cloudy periods). The data cover about 40% of the observation period of each sunspot.

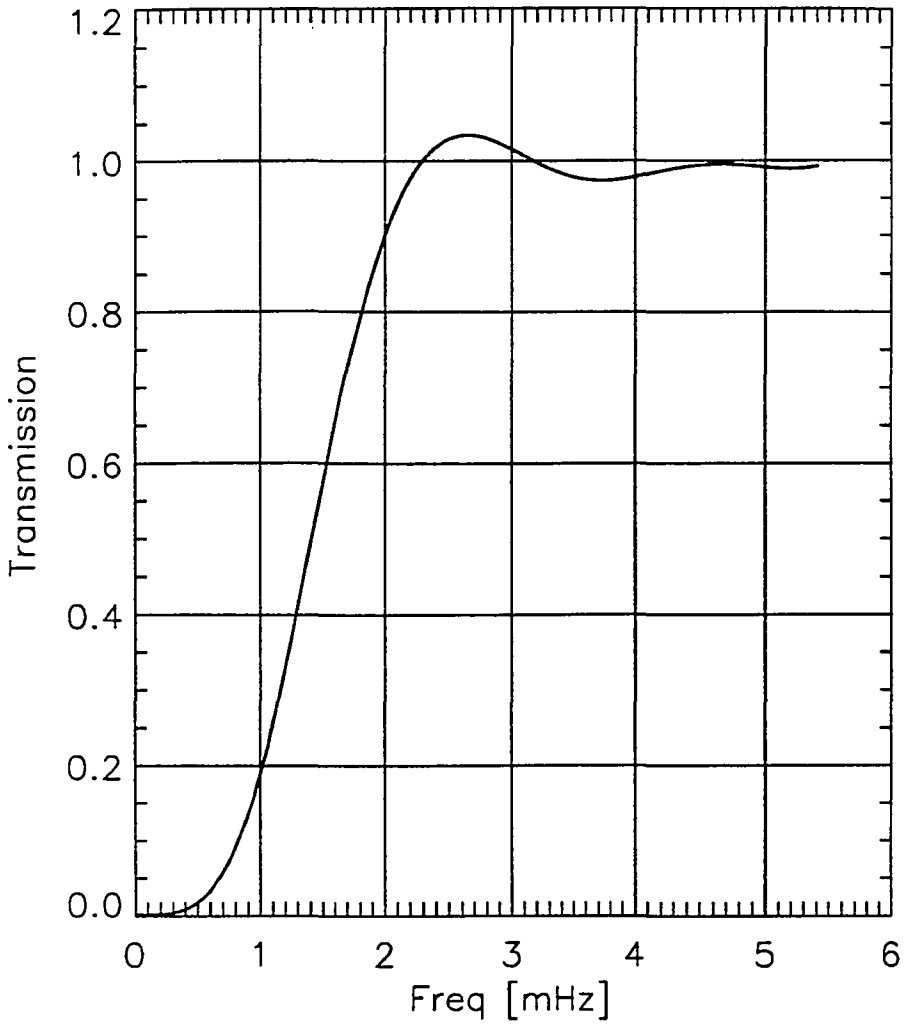

Figure 3.03 Transmission profile of the temporal filter used on the velocity time series. The Gaussian coefficients of the running mean calculations produce a smoothly varying frequency transmission with few ripples at high frequencies.

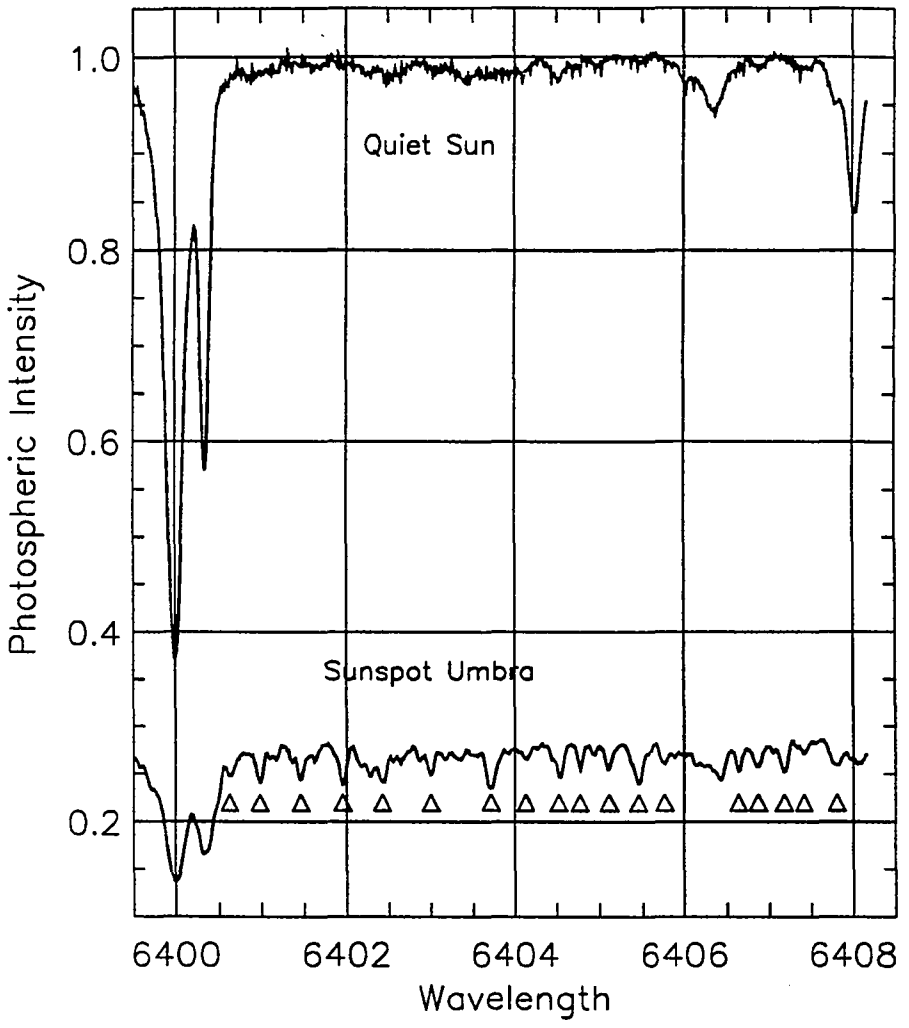

Figure 3.04 Sample photospheric and umbral spectra are shown in this plot. The pure umbral lines are marked with triangles; the two absorption lines at the left are two Fe I absorption lines which are prominent in the photosphere. See Table 3.3 for more information about these lines.

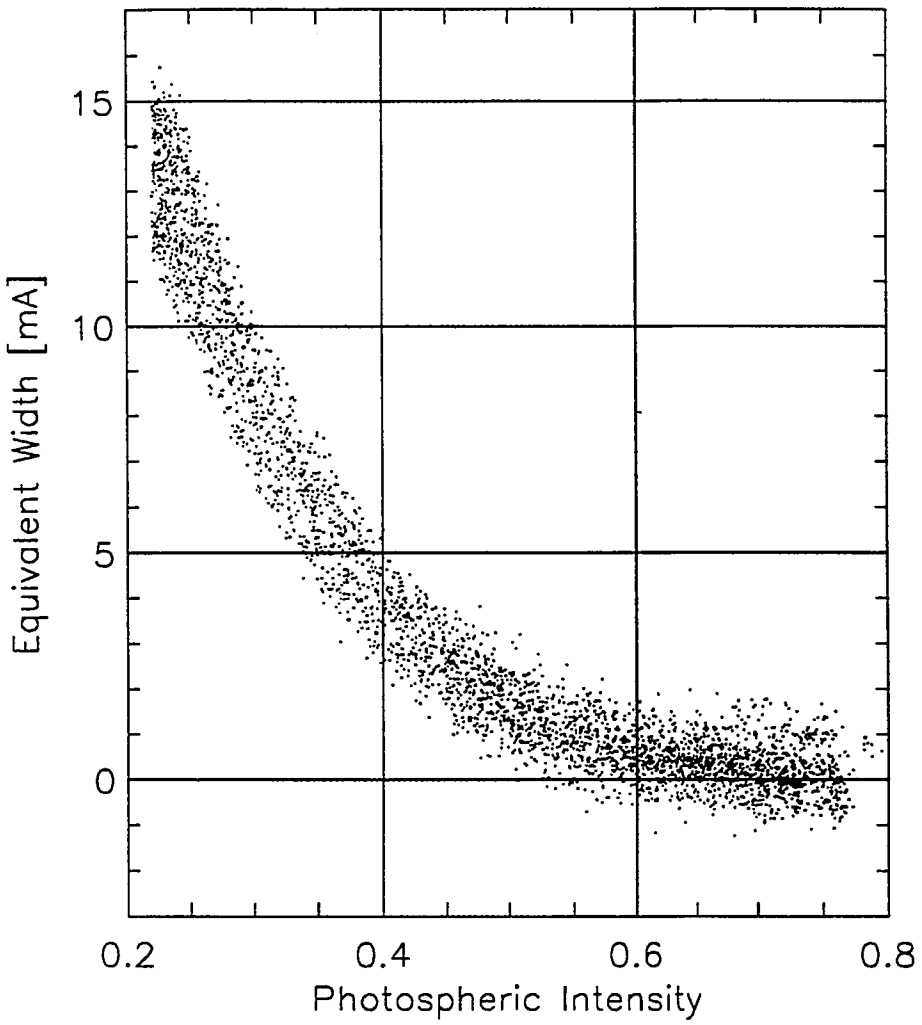

Figure 3.05 The equivalent width as a function of continuum intensity for a TiO/CN molecular absorption line at λ6405.45Å in NOAA 6619. The equivalent width is a strong function of the continuum intensity which is a crude measure of the temperature. The scatter is from two sources: (1) stray light influences the intensity level and (2) the photon statistics of the detector give an expected noise of ±0.5mÅ in the equivalent width.

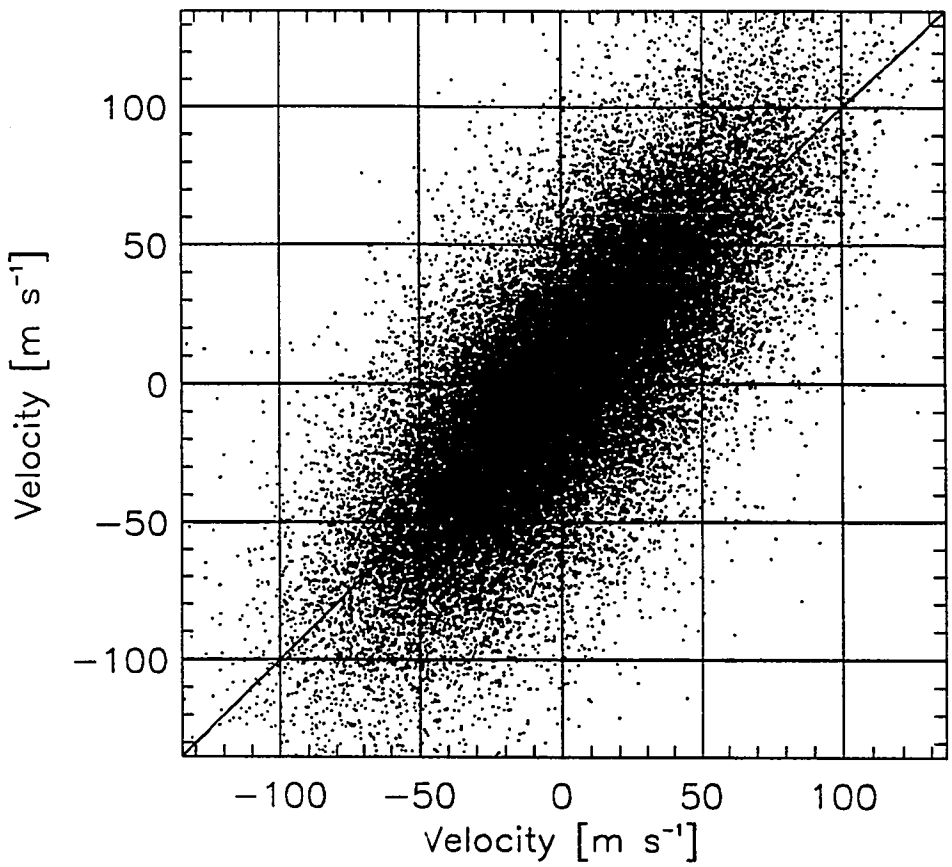

Figure 3.06 A comparison of the velocity computed from two sets of umbral lines. The velocities are well correlated along a line with a slope of one with a scatter of about ±20 m s^{-1}. This scatter probably originates solely from measurement error in the line shift computation; there is no evidence for a phase shift between these two sets of velocities.

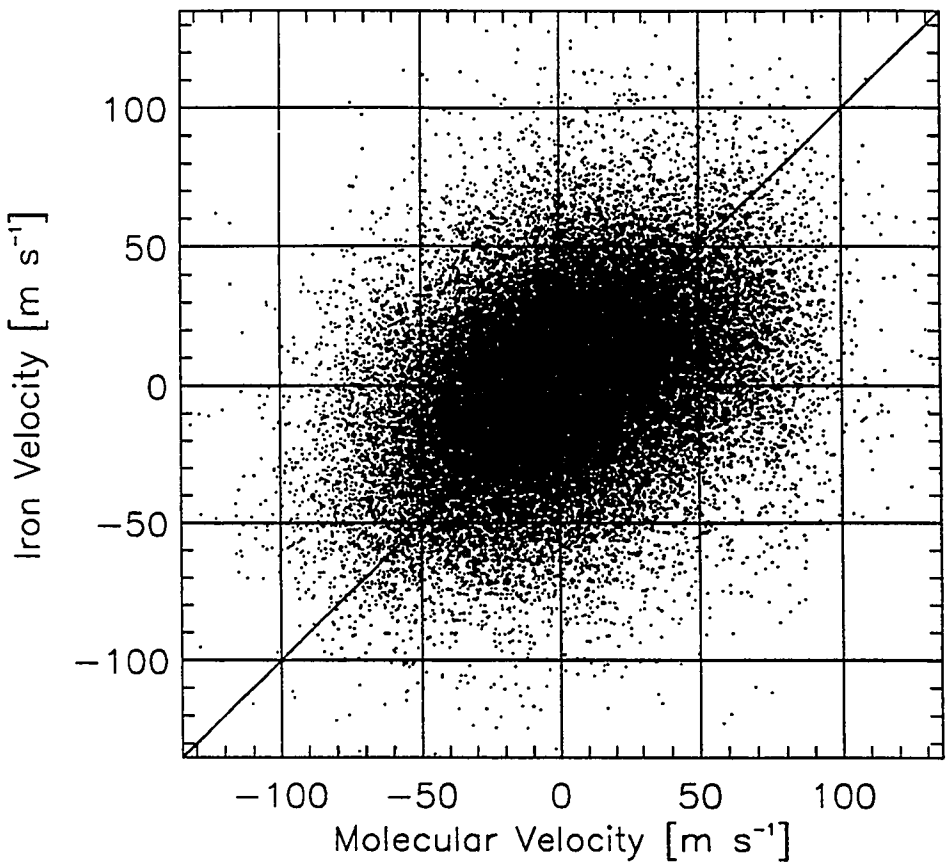

Figure 3.07 A comparison of the velocity computed from the pure umbral absorption lines with the velocity computed from the Fe I absorption lines. These velocities are not well correlated; this suggests that the two measurements probe different velocity fields. The Fe I velocity may be contaminated by quiet-sun oscillations or there may be a phase shift between these two velocities.

Figure 3.08 A plot of some of the Bessel masks used in the Fourier-Bessel analysis of NOAA 6625 (see text). Here we plot the real component of the normalized $\tilde{M}_{m,n}(r,\theta)$ for $m = 0,5$ and $n = 1,4$; for clearity we have expanded the radial dimension by a factor of four.

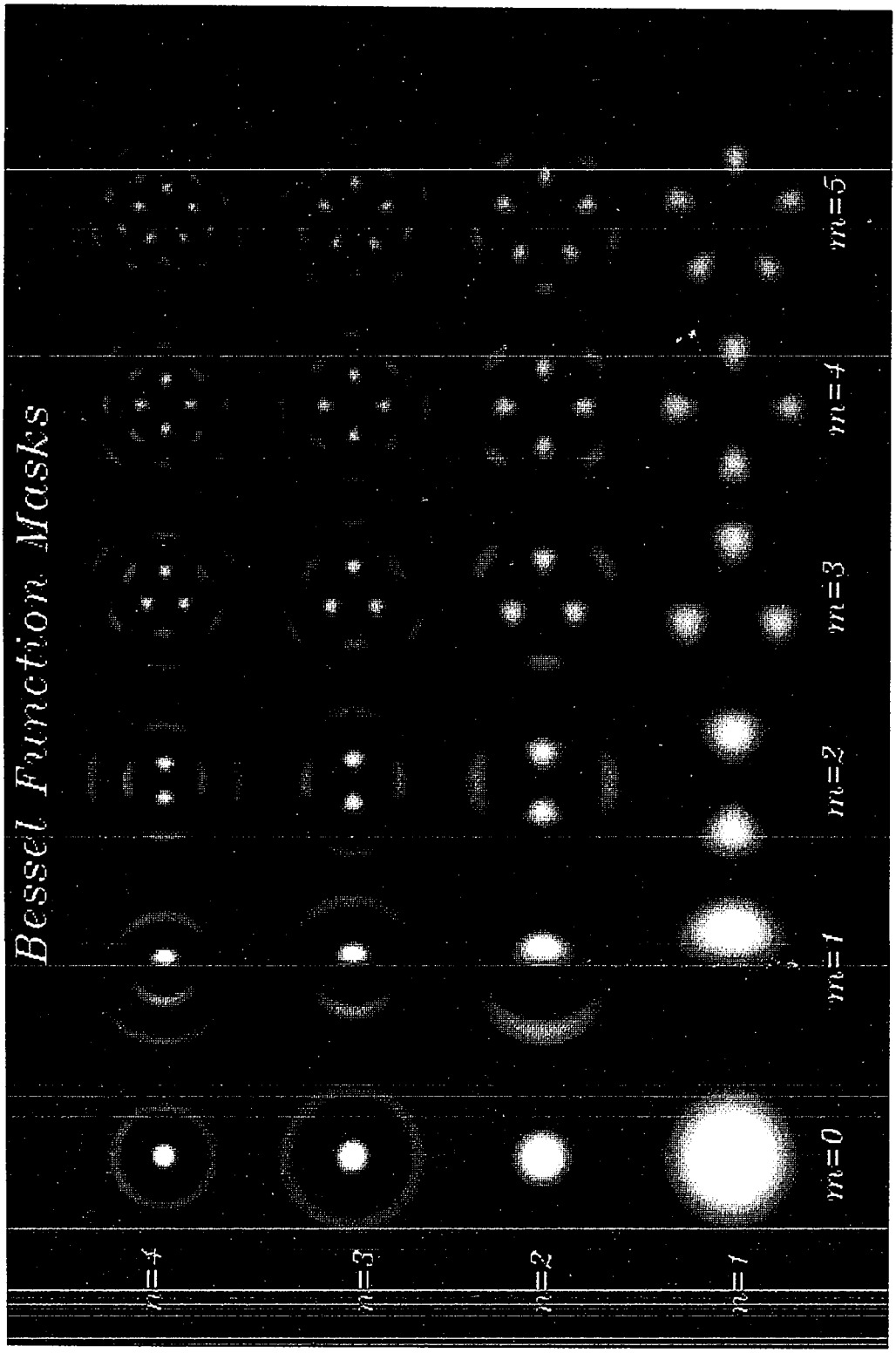
Bessel Function Masks
m=0
m=1
m=2
m=3
m=4
m=5
n=4
n=3
n=2
n=1

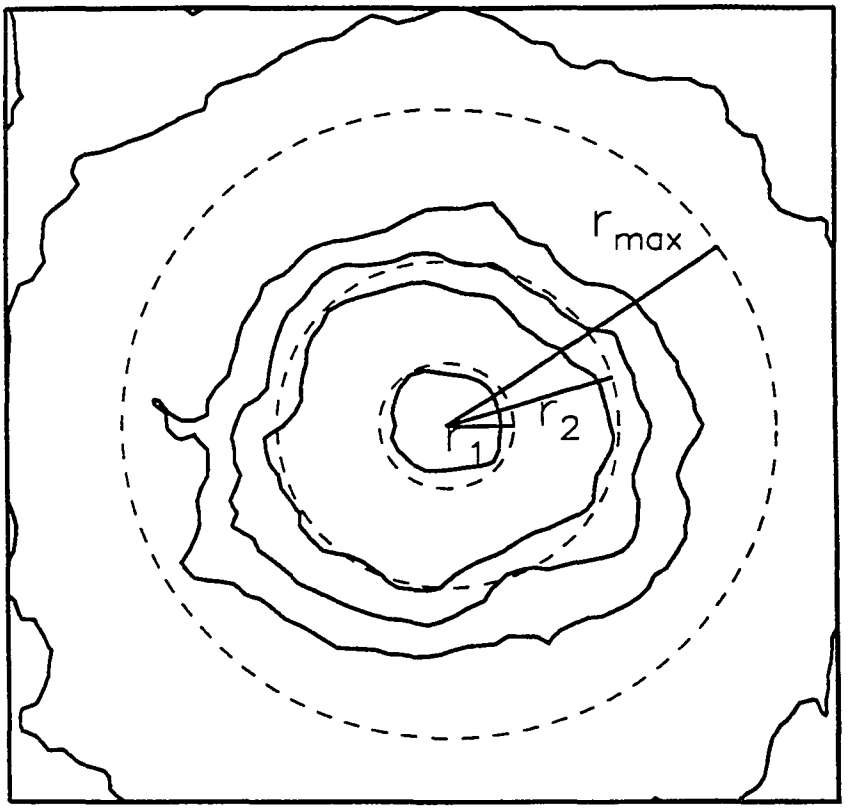

Figure 3.09 The pattern of concentric disks used for the $\alpha(r)$ calculations. Each disk covers a larger area, until the disk with radius r_{umbra} covers the whole umbra. Disks are used because it would be impossible to distinguish ingoing from outgoing traveling waves using annular regions.

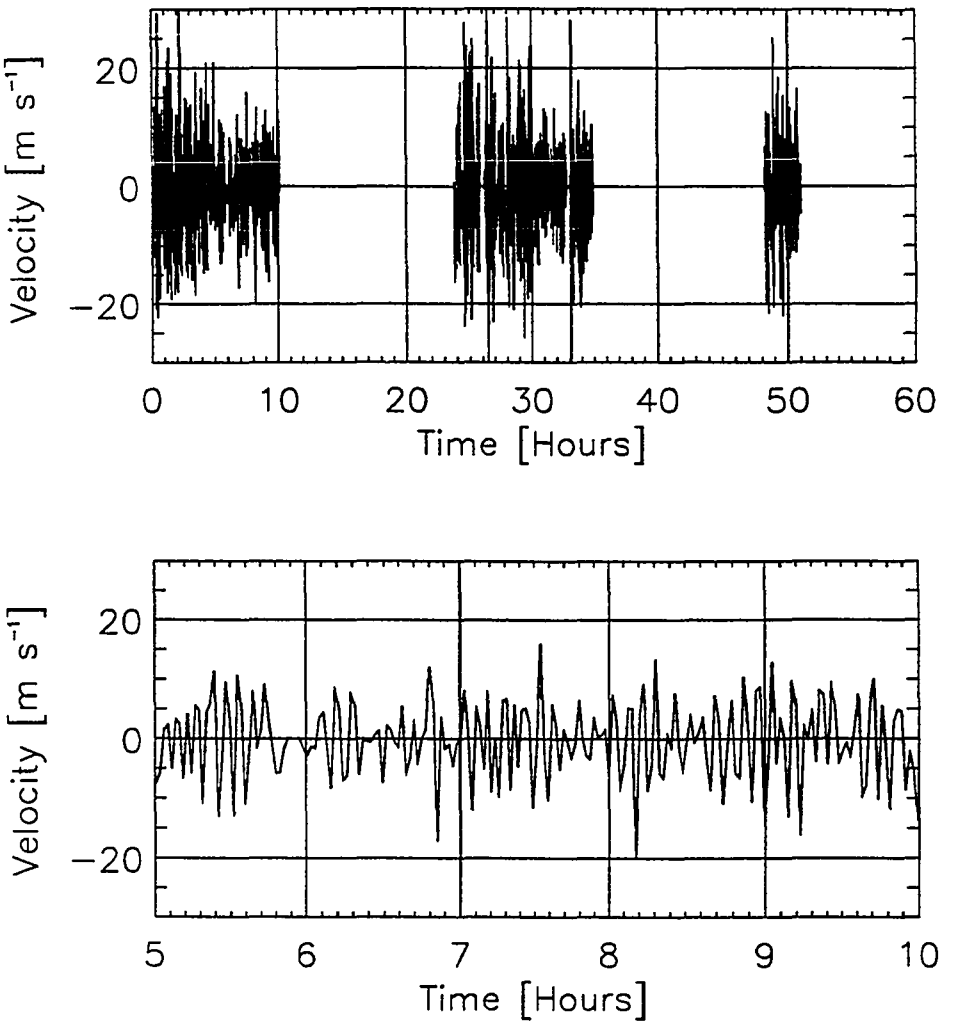

Figure 3.10 The mean umbral velocity for the observations of NOAA 6625. The top figure shows the whole data set, while the bottom figure illustrates a three hour segment. In the lower graph we see the period is roughly five minutes; in both figures a slow beating pattern is clear.

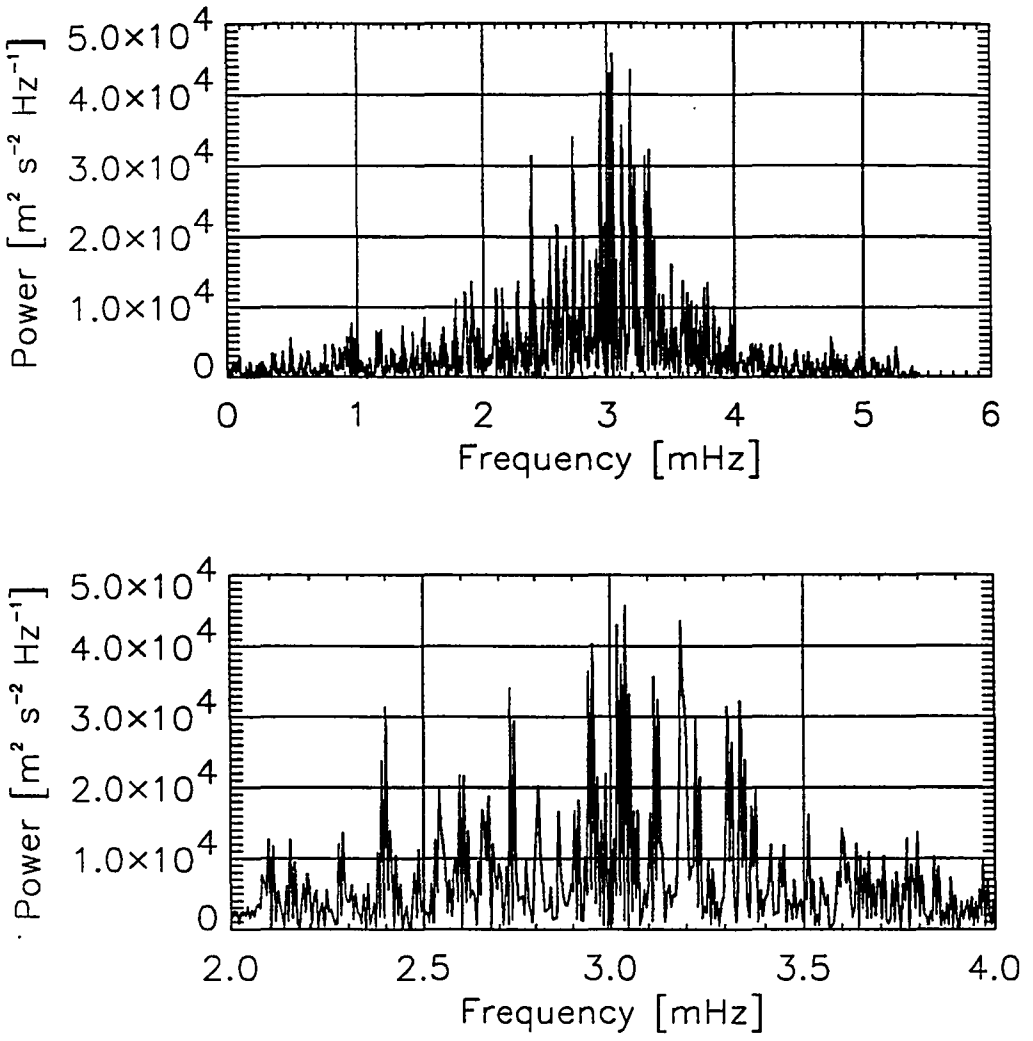

Figure 3.11 The power spectrum of the mean umbral velocity for NOAA 6625. The whole spectrum is shown in the top figure, and the five-minute period band is shown below. The resolution is $\Delta\nu = 5.4\mu$Hz, but there are no well resolved peaks.

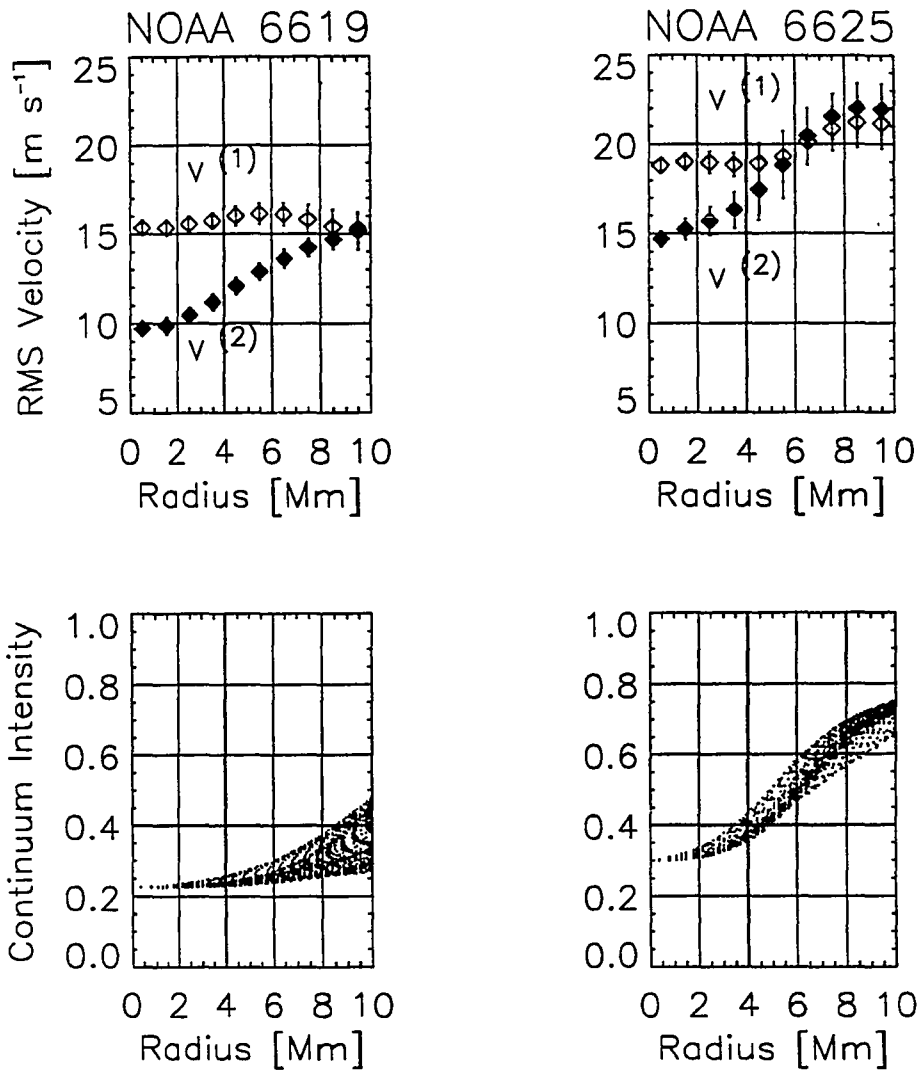

Figure 3.12 Oscillation velocity in the inner umbral regions. The upper figures show the RMS velocity inside the inner regions of the sunspot umbrae. The open symbols show the RMS velocity integrated over all spatial wavenumbers $V^{(1)}_{RMS}$; the filled symbols show the RMS velocity with the lowest spatial wavenumber removed $V^{(2)}_{RMS}$. Note that the high wavenumber velocity decreases toward the umbral center. It is likely that this reflects the decreasing amplitude of an acoustic wave being absorbed as it crosses the sunspot umbra. The lower figures show the continuum intensity as a function of radius for the same regions.

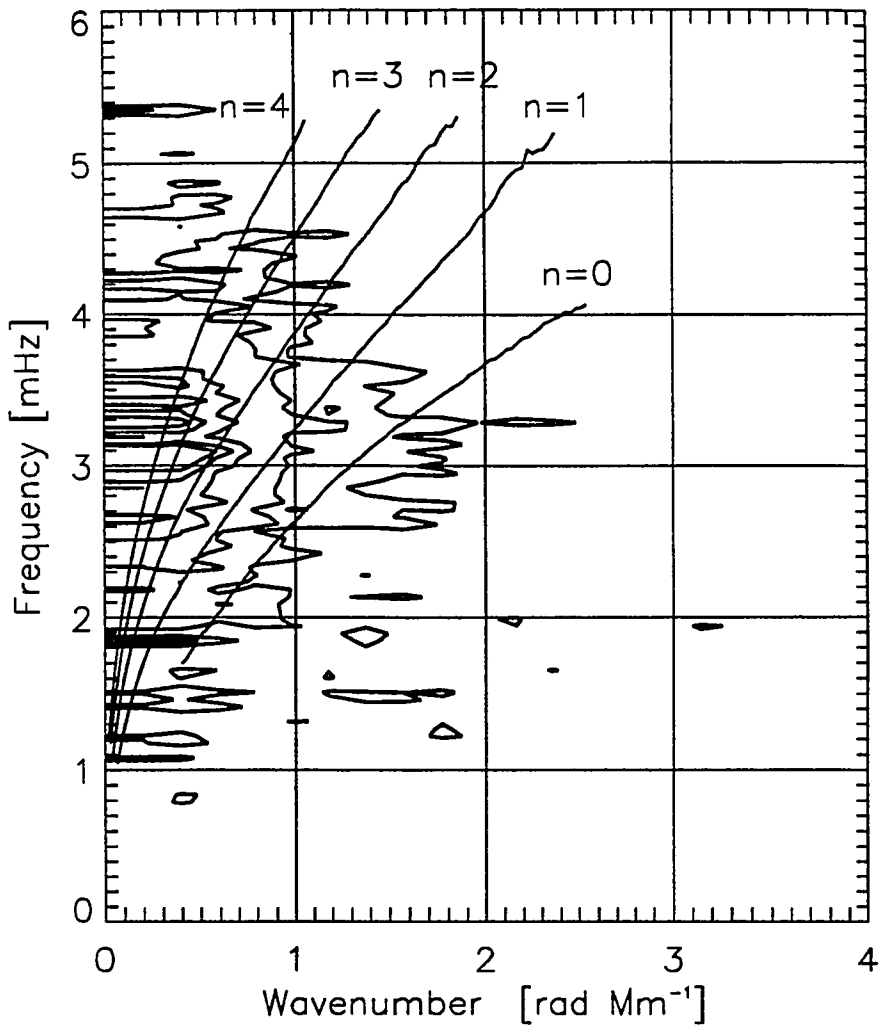

Figure 3.13 Diagnostic (k,v) diagram for the umbral oscillations of NOAA 6619. This diagram has very poor spatial resolution due to the small size of the sunspot umbra. The data has been binned in temporal frequency by a factor of 100 for purpose of display. The power has been divided by fits to the spatial and temporal power gradients. The umbral oscillation power is consistent with the global p-mode power, as can be seen with the comparison with global p-mode ridges also shown (Libbrecht and Kaufman). There are no prominent spatial or temporal resonant frequencies seen in the data. A Fourier-Bessel analysis of the data shows consistent results; no prominent resonant frequencies are resolved.

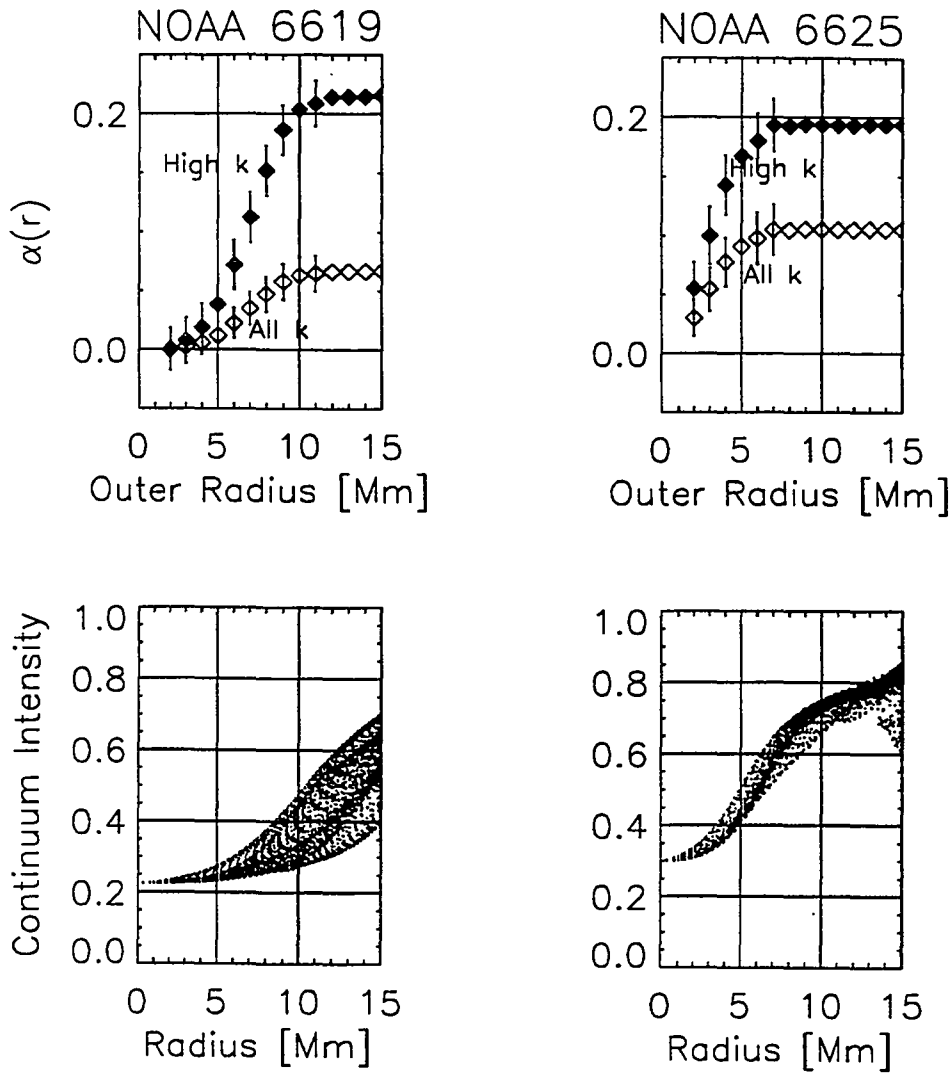

Figure 3.14 Acoustic absorption inside the sunspot umbrae. The top figures show the absorption function for both sunspot umbrae. The open symbols represent the absorption function integrated over all spatial wavenumbers $0 \leq k < 6.2$ [rad Mm^{-1}]; the filled symbols show the absorption excluding the lowest wavenumber bin, $0.2 \leq k < 6.2$ [rad Mm^{-1}]. The function represents a radially integrated absorption rather than the acoustic absorption at a particular radius within the umbra. This integrated absorption increases from zero in the umbral centers to a value of roughly 0.2 at the outer edge of the umbrae; the constant values outside the umbra merely reflect the lack of velocity data there. The absorption function which includes all spatial wavenumbers has a significantly lower peak value since the stationary power is included in the analysis. Finally, the lower two figures show the continuum intensity versus radius and illustrates the extent and symmetry of the sunspot umbrae.

APPENDIX A

Alignment of the Spar Polar Axis

The fast guiding system of the MCCD instrument required new spatial stability of the solar image on the spectrograph slit. Several adjustments to the coronagraph telescope and the spar mounting were made (see Chapter 2 for details). In this Appendix we describe the measurement and re-pointing of the polar axis of the spar mounting.

1. Data Collection

On several days in July and October 1988 the declination error signal from the guider circuit was recorded with the aim of checking and correcting the alignment of the spar's polar axis. An up/down counter was connected to the circuit adding north driving pulses and subtracting south driving pulses, and thus providing an integrated pulse count throughout the day. This count was manually recorded at approximately 20 minute intervals. The count was not stable on short time scales; it varies over a range of values with a period between 5 and 20 seconds. This range was recorded and the average of this range was defined to be the count value. The proper motion of the Sun which should dominate this error signal is in a southerly direction; but the signals increase during each day. This implies that actually north driving pulses were subtracted from south driving pulses contradicting signal labels on the guider circuit schematics. In the reduction of the data this sign error was taken into account.

2. Data Reduction

First proper solar motion was removed from the declination error signal using the solar declination values computed from an ephemeris program. This simple subtraction inherently assumes no misalignment; a rigorous routine would map the true solar motion into the rotated telescope coordinate system, and then subtract the apparent motion. Such an iterative routine may be necessary if higher order errors (such as spar flexure) are to be studied. Next a simple algorithm was used to remove refraction between 18 hours and 03 hours UT, when the solar altitude was greater than 15 degrees; only this 9 hour segment of the daily data was used in further analysis. The guider data can provide detailed information about atmospheric refraction but the polar alignment problem can be adequately studied without such knowledge.

Finally, the data segment was fit to an error function to determine the altitude and azimuth errors of the spar's polar axis. We define a coordinate set with $\hat{x}$ directed towards the celestial equator at the meridian, $\hat{y}$ directed towards the eastern horizon, and $\hat{z}$ directed at the north celestial pole. We perform three rotations, (1) first about $\hat{y}$ by an angle l equal to the observer's latitude, (2) next about $\hat{x}'$ by an angle ε equal to the azimuthal pointing error of the spar mount, and finally (3) about $\hat{y}''$ by an angle $-(l+\eta)$ equal to the observer's latitude plus the elevation pointing error of the spar mount (η). This gives us the matrix equation:

$$\begin{bmatrix} x''' \\ y''' \\ z''' \end{bmatrix} = \begin{bmatrix} \cos(l+\eta) & 0 & -sin(l+\eta) \\ 0 & 1 & 0 \\ \sin(l+\eta) & 0 & \cos(l+\eta) \end{bmatrix} \begin{bmatrix} 1 & 0 & 0 \\ 0 & \cos(\varepsilon) & \sin(\varepsilon) \\ 0 & -sin(\varepsilon) & \cos(\varepsilon) \end{bmatrix} \begin{bmatrix} \cos(l) & 0 & \sin(l) \\ 0 & 1 & 0 \\ -sin(l) & 0 & \cos(l) \end{bmatrix} \begin{bmatrix} x \\ y \\ z \end{bmatrix} \qquad \text{(A1)}$$

Given this system the apparent declination of an object δ' is given by

$$\delta' = \frac{\pi}{2} - \cos^{-1}(z''') \tag{A2}$$

and finally the declination guider error is

$$\Delta(t) = \delta(t) - \delta'(t) \tag{A3}$$

The error function must include an arbitrary zero point since the subtraction of the proper solar motion was done arbitrarily simply by assuming no declination error at the first data point of each set. The fits to the July 1988 data are shown in Figure A1. The positions of the spar polar axis in the sky are plotted in Figure A2.

The errors in the altitude and azimuth fit parameters were determined for the 30 Oct fit. The 99% confidence levels were estimated from a contour plot of constant χ^2 values in altitude-azimuth parameter space. The values were ± 4.1" in altitude, and ± 2.1" in azimuth; these values prove to be small compared with the spurious pier axis motions as can be seen in Figure A2.

3. Pier Motion

The azimuth of the pier was first adjusted on 28 July. Measurements taken from the pier showed that the adjustment bolts have a lever arm of about 70 cm, and the bolts had about 5.8 threads per cm. These values suggested that a 42 degree rotation of each bolt would achieve a polar axis azimuth shift of 54 arcseconds.

Unfortunately, the adjustments are not as straightforward as stated above; corrections to the polar alignment were done iteratively. As seen in Figure A2, the elevation of the polar axis varied quite a good deal, though the pier elevation screws were

not adjusted. This figure also shows creeping of the pier, since no adjustments were made to the pier between 29 July and 30 July. The mechanical stresses involved in moving the pier are complex so iterative alignments are required.

4. Current Alignment of the Mees Spar

From Figure A2 we can see that the spar currently points 44 arcseconds south of the North Celestial Pole. What types of spurious image motion will this misalignment produce? No image translation will result; the spar autoguider will track the disk center properly throughout the day. However, a spurious image rotation will be introduced. Since the apparent motion of the Sun through the sky differs from its true motion, the implied rotation rate will also differ from the true rotation rate. For a simple altitude error in the polar axis the spurious rotation will vary like $a_0\cos(H.A.)$, where a_0 is the altitude error, and $H.A.$ is the solar hour angle. The average rotation rate is then $a_0/6$ arcseconds per hour. With a_0 equal to 44 arcseconds, the spurious rotation rate is $3.4x10^{-5}$ rad hour^{-1}. Since the solar image radius is about 1000 arcseconds, this results in a maximum image displacement of 0.04 arcseconds per hour. This small displacement is impossible to detect with the Coude spectrograph.

5. Daily Image Motion

As a side note to the alignment project the guider signal variation can be used to determine the guider-induced image motion. Figure A3 shows a plot of the error signal variation for the July data. The minimum image motion induced by the guider

is about 1 arcsecond, between the hours of 22 and 24 UT. This behavior differs from typical seeing effects at Mees, which provide the most stable atmosphere in the morning hours of each day. The guider motion is directly transferred to all telescope images and should be removed. Gain adjustment of the guiding feedback loop may reduce this motion. However, wind shake of the spar, or thermal effects in the dome may perpetrate this motion; these problems are much more difficult to fix.

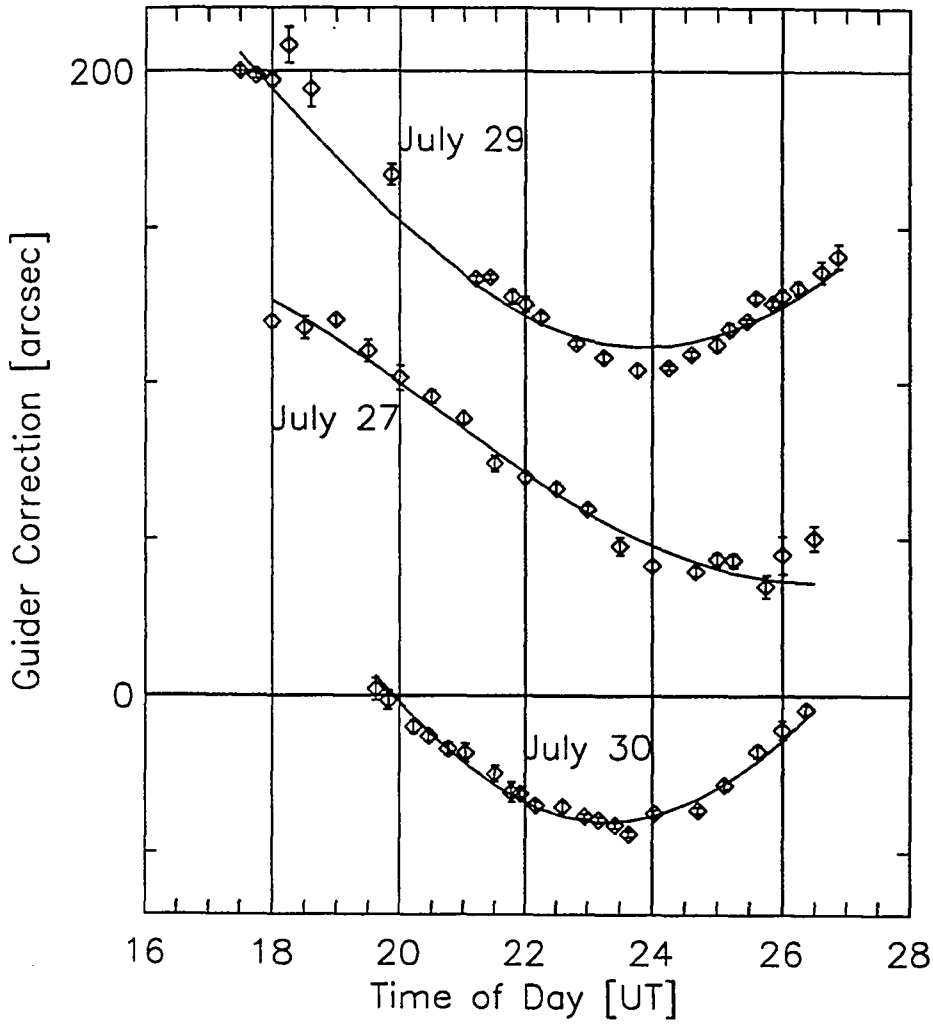

Figure A1 Fits to the Guider Correction Signal. This figure shows the guider correction signal as measured in July 1988 along with fits to the data points using the error function given in the text. The error bars on the data points mark the measured range of guider signal measurements.

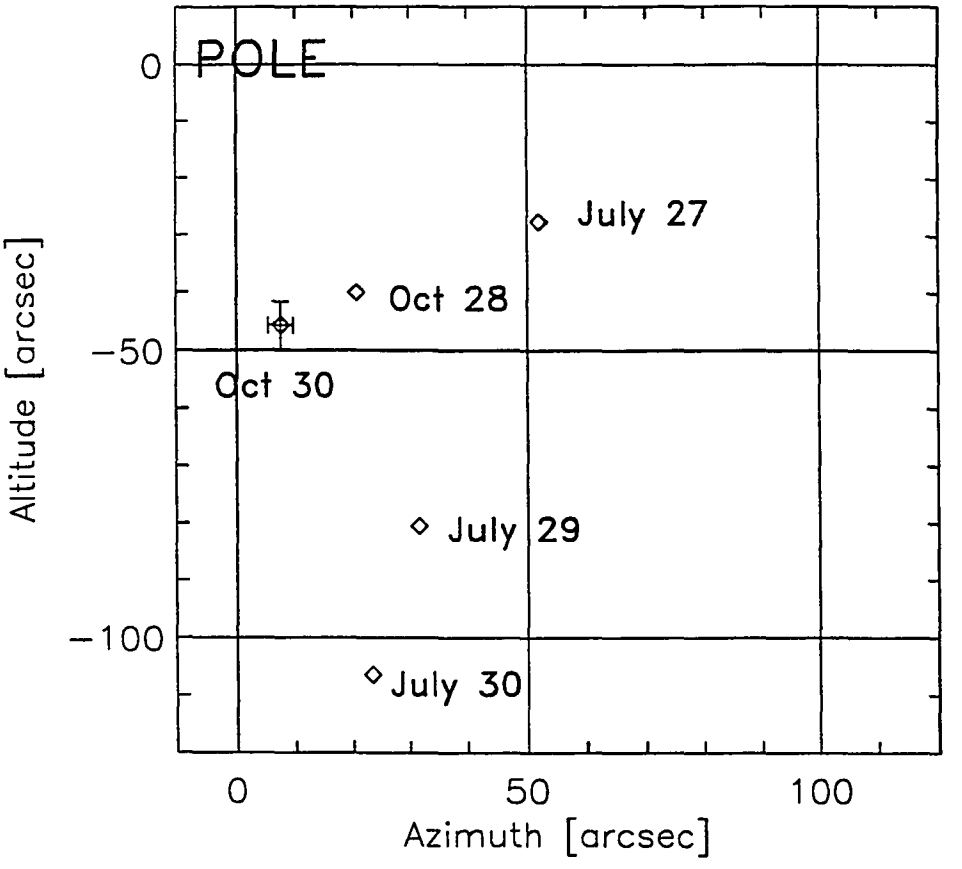

Figure A2 The Pointing of the Axis of the Solar Spar. The azimuth and altitude errors computed by fits to the data from July and October 1988 are plotted in this diagram along with the true position of the North Celestial Pole. The error bars on the 30 Oct point represent 99% confidence level of the fit to the data points. Note that the spar axis altitude was never directly adjusted; motion in this direction results from mechanical complications while adjusting the azimuth.

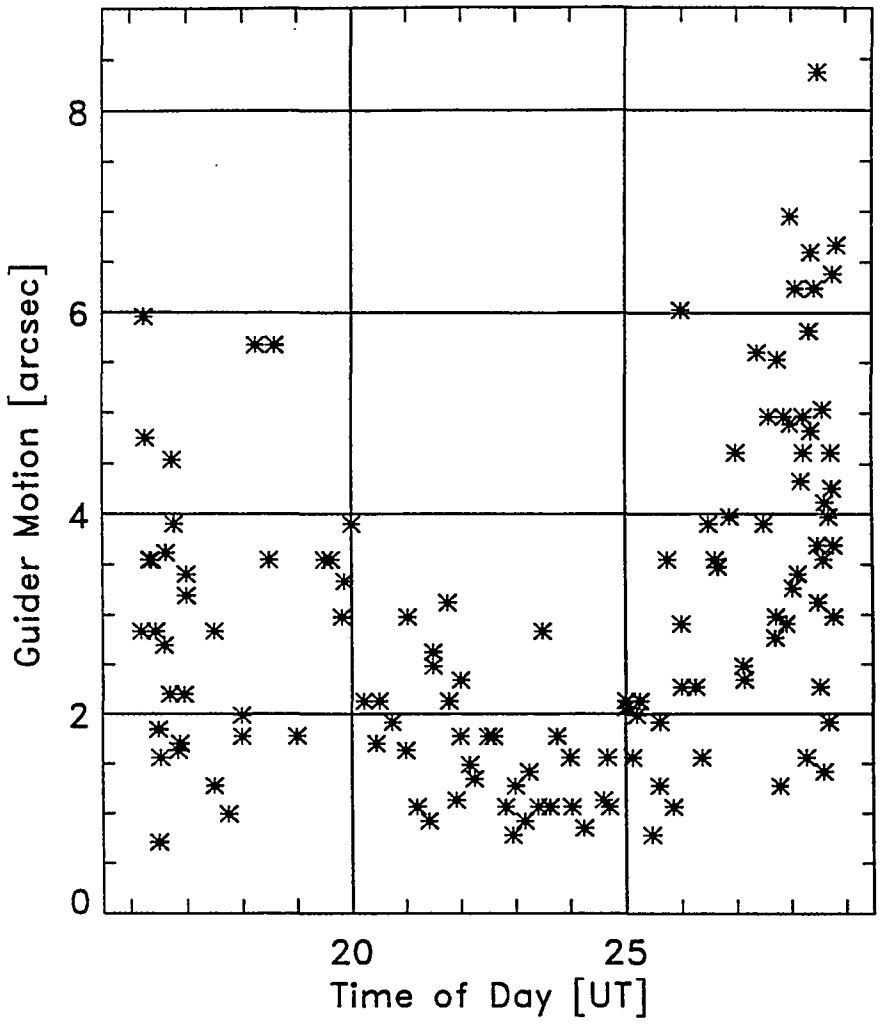

Figure A3 The Daily Motion of the Spar Pointing. On this figure we plot the range of spar positions recorded during the July 1988 measurements. The spar oscillated about a mean position by the range denoted on this graph with a period of between 10 and 60 seconds. Note that when the spar is vertical near local noon (22:30 UT) the oscillatory motions reach a minimum.

APPENDIX B

Determining the Umbral Acoustic Opacity from Traveling Wave Analysis

As in Chapter 3 we can define an acoustic opacity $\chi(r)$ with the equation

$$\frac{dP(r)}{P(r)} = -\chi(r)dr \tag{B.1}$$

At a given radius r, we can express the ingoing wave power $P_-(r)$ and the outgoing wave power $P_+(r)$ in terms of the total incident wave power P_i with the following integral equations:

$$P_-(r) = P_i \; e^{-\int_r^{r_{umbra}} \chi(r')dr'} \tag{B.2}$$

$$P_+(r) = P_i \; e^{-\int_0^r \chi(r')dr'} \; e^{-\int_0^{r_{umbra}} \chi(r')dr'} \tag{B.3}$$

where r_{umbra} is the radius of the umbra. (Note that the outgoing wave is attenuated by an extra factor since it enters from the opposite side of the umbra.) We assume the attenuation of the waves is small, and can then use a Taylor series expansion about zero for the exponential functions and only keep linear terms. Since we know that the absorption is on the order of 20%, this assumption is legitimate for our purposes. The Taylor expansion leads to the following expressions:

$$P_-(r) \approx P_i \left[1 - \int_r^{r_{umbra}} \chi(r')dr'\right] \tag{B.4}$$

$$P_+(r) \approx P_i \left[1 - \int_0^r \chi(r')dr' - \int_0^{r_{umbra}} \chi(r')dr'\right] \tag{B.5}$$

Now we express the absorption function $\alpha(r)$ in terms of the ingoing and outgoing wave components. The mean ingoing and outgoing power at a radius r can be expressed as:

$$P_{in}(r) = \frac{1}{r}\int_0^r P_-(rprime)dr' \tag{B.6}$$

$$P_{out}(r) = \frac{1}{r}\int_0^r P_+(rprime)dr' \tag{B.7}$$

We substitute the appropriate expressions, integrate by parts, and take the difference (equating the expressions P_i with $P_{in}(r_{umbra})$ which both represent the total incident power) to arrive at an expression for the absorption function

$$\alpha(r) \equiv \frac{P_{in}(r)-P_{out}(r)}{P_{in}(r_{umbra})} = 2\int_0^r (1-r/r)\,\chi(r)dr \tag{B.8}$$

Finally substituting the simplest solution for the acoustic absorption, a constant term $\chi(r) = \chi_0$, leads us to the solution

$$\alpha(r) = \chi_0 r \tag{B.9}$$

Using a linear fit to the absorption functions for NOAA 6619 and NOAA 6625 results in a value of $\chi_0 \approx 0.03$ Mm^{-1}